Promoting Active Sites for Hydrogen Evolution in $MoSe_2$ via Transition-Metal Doping

Akash Jain,[1] Maya Bar Sadan[2,3] and Ashwin Ramasubramaniam[4,*]

[1] Department of Chemical Engineering, University of Massachusetts, Amherst, MA 01003, U.S.A.

[2] Department of Chemistry Ben-Gurion University of the Negev, Beer-Sheva 8410501, Israel

[3] Ilse Katz Institute for Nanoscale Science and Technology, Ben-Gurion University of the Negev, Beer-Sheva 8410501, Israel

[4] Department of Mechanical and Industrial Engineering, University of Massachusetts, Amherst, MA 01003, U.S.A.

ABSTRACT

Molybdenum diselenide ($MoSe_2$)—a transition metal dichalcogenide—is a promising non-precious metal catalyst for the hydrogen evolution reaction (HER). However, practical application of $MoSe_2$ for electrocatalytic HER is hindered by its poor electrical conductivity, high overpotential, and the limited number of active sites. Specifically, while the edges of $MoSe_2$ are highly active for HER, the basal plane, which constitutes most of the catalyst surface, is inert towards HER. While prior studies have focused on improving the activity of $MoSe_2$ either by promoting the formation of highly active basal-plane Se vacancies or by substitutional doping of metal atoms, the interaction between dopants and Se vacancies—whether beneficial or detrimental towards HER—has not been fully understood. Here, we employ density functional theory calculations to study the interplay between prototypical transition-metal (TM) dopants (Mn, Fe, Co, and Ni) and Se vacancies, and the consequent influence on hydrogen adsorption (a descriptor

of HER activity in acidic media) at basal planes, edges, and Se vacancy sites. We correlate trends in the free-energies of hydrogen adsorption and Se vacancy formation with changes in the electronic structure of $MoSe_2$ upon TM doping as well as structural changes arising due to TM dopant atoms. Broadly, our studies show that the studied electron-rich TM dopants favorably modify the electronic structure of $MoSe_2$ basal planes towards HER and, additionally, electrochemical generation of Se vacancies becomes more facile on doped basal plane and edges at smaller cathodic potentials. These newly formed Se vacancies are typically highly active towards HER and substitutional doping can be viewed as an avenue for defect-mediated activation of $MoSe_2$.

Corresponding Author

* ashwin@engin.umass.edu

1. INTRODUCTION

Hydrogen gas (H_2) is highly desirable as a clean fuel and electrochemical water splitting (EWS) is believed to offer a renewable and sustainable route for H_2 production.[1,2] In EWS (in acidic media), H_2 gas is generated at the cathode via the hydrogen evolution reaction (HER) in which two protons and electrons combine to form molecular hydrogen gas [$2H^+_{(aq)} + 2e^- \rightleftarrows H_{2(g)}$].[3] For scalable EWS, new HER catalysts are required to replace expensive platinum (Pt), which still remains the electrocatalyst of choice due to its low overpotential, fast HER kinetics, and high electrical conductivity.[3–5] Apart from the high cost and scarcity of Pt, other operational problems such as catalyst corrosion, sintering, and poisoning pose limitations for large scale H_2 production,[6,7] further motivating the search for alternative HER electrocatalysts. Along these lines, two-dimensional (2D) transition metal dichalcogenides (TMDs) such as molybdenum and tungsten disulfides and diselenides have emerged as promising electrocatalysts for HER due to their highly active edges.[8–16] In particular, $MoSe_2$ is a promising candidate due to its higher electrical conductivity and smaller HER overpotentials than MoS_2, WS_2 and WSe_2.[11,12,17–20] Hence, in this work we focus on modifying $MoSe_2$ electrocatalyst for HER. In general, 2D TMDs have lower electrical conductivity, higher overpotentials, and more sluggish HER kinetics relative to Pt. More importantly, the active edge sites of these 2D sheets comprise only a small fraction of the total exposed surface, limiting the overall electrochemical active surface area of the catalyst. The basal planes, which constitute most of the catalyst surface, are generally inert towards HER, [9,21,22] although chalcogen vacancies and other defects in the basal plane can potentially serve as active sites.[22–27]

To overcome the shortcomings of TMDs as HER catalysts, several experimental studies have proposed strategies like morphology engineering to maximize active edges in the catalyst,

supporting TMDs on more conductive supports, modification with heteroatom doping, and defect and phase engineering.[8,11,12,22,28–30] Specifically, for $MoSe_2$, it was demonstrated that increasing the concentration of Se vacancies improves its HER activity.[23,26,27,31,32] Different morphologies for the catalyst were also suggested, for instance, vertically aligned $MoSe_2$ films grown perpendicular to planar and curved substrates,[11,12] $MoSe_2$ in nanoflower architectures,[33,34] and porous $MoSe_2$ nanosheets,[35] all of which were aimed at exposing active edges sites. Furthermore, it was shown that introducing the metastable 1T metallic phase within the thermodynamically stable semiconducting 2H phase of $MoSe_2$ improves the electrical conductivity and HER kinetics,[36–38] as does supporting $MoSe_2$ on graphene-based materials.[39–41] $MoSe_2$ has also been modified through heteroatom doping with sulfur[42,43], nitrogen[37], boron [44] and transition metals (W, Mn, Co, Ni, Ru, Zn)[33,34,45–51] resulting in a larger catalytic active area, lower overpotentials, faster HER kinetics, and better electrical conductivity than undoped $MoSe_2$. However, there are as yet only a few theoretical studies[33,34,44,46–48] that provide fundamental insights into the mechanisms that underlie the aforementioned reports of improved activity of engineered and/or modified $MoSe_2$ systems. Furthermore, most DFT studies on heteroatom-doped $MoSe_2$—the focus of this paper—have employed doped basal-plane models to justify the improved HER performance of $MoSe_2$ even though the catalyst is Se-deficient (defect rich) in practice with multiple exposed edges; a couple of exceptions are the work of Gao *et al.*[44] and Kuraganti *et al.*[33] who studied both basal planes and edges of B-doped and Mn-doped $MoSe_2$ catalysts, respectively, via density functional theory (DFT) modeling.

In this work, we employ DFT modeling to investigate and compare systematically the influence of select earth-abundant transition metal (TM) dopants, namely, Mn, Fe, Co and Ni on the structure, the thermodynamics of electrochemical Se vacancy formation, and the HER activity of

$MoSe_2$ in acidic media. We selected these dopants because recent experimental studies have shown that Mn-, Co-, and Ni-doped $MoSe_2$ electrocatalysts possess significantly improved HER activities over undoped $MoSe_2$ electrocatalyst.[33,46] Furthermore, this series of 3*d* TM dopants allows for the sequential introduction of excess electrons into the conduction band of $MoSe_2$, thereby allowing for fundamental insights into the connection between electronic structure and HER activity. We study the change in free-energy of hydrogen (H) adsorption, ΔG_H,—a well-established descriptor of HER activity in acidic media—at pristine sites and Se vacancy (V_{Se}) sites on undoped as well as TM-doped basal planes, Mo-edges, and Se edges. We also report the energy required to form Se vacancies via the electrochemical deselenization reaction (DSR), ΔG_{DSR}, on undoped as well as TM-doped basal planes, Mo edges, and Se edges; such electrocatalytic formation of chalcogen vacancies has been reported recently as a source of activity enhancement in MoS_2 [22,52,53] and has not yet been systematically studied for $MoSe_2$. We explain the trends observed in ΔG_H and ΔG_{DSR} by correlating these reaction free energies with changes in the electronic structure as well as the structural distortions induced by dopants and adsorbed H. Finally, using a volcano plot correlation between HER activity and hydrogen binding energies, we identify potentially HER active sites on TM-doped $MoSe_2$. Broadly, our studies show that the introduction of excess electrons in $MoSe_2$ via TM doping renders the inert semiconducting basal plane of $MoSe_2$ more favorable towards H-adsorption. Additionally, electrochemical generation of Se vacancies becomes more facile on doped basal planes and edges at smaller cathodic potentials. In general, Se vacancies in TM-doped $MoSe_2$ are highly active for HER and TM doping can be viewed as a promising route for activating $MoSe_2$ electrocatalysts by promoting Se vacancy defect formation.

2. COMPUTATIONAL METHODS

The Vienna Ab Initio Simulation Package (VASP; version 5.4.1) [54,55] was used for DFT calculations, all of which were performed with spin polarization to account for unpaired electrons of the dopant atoms. The projector-augmented wave (PAW) method [56,57] was used to describe core and valence electrons along with the Perdew-Burke-Ernzerhof (PBE) generalized gradient approximation (GGA) [58] for the description of electron exchange and correlations. The cutoff energy for the plane-wave basis set was 400 eV and Gaussian smearing of 0.05 eV was used for integrations over the Brillouin zone. The conjugate-gradient algorithm was used for structural optimizations of all DFT models with a Hellman-Feynman force tolerance of 0.01 eV/Å. During structural optimization, positions of all atoms were updated while the supercell dimensions were held fixed. Relaxing the cell vectors changed the total energy and supercell dimensions of monolayers (MLs) by $\pm$20 meV and $\pm$0.5%, respectively, which are within the expected error of the numerical method; moreover, relaxing cell vectors was found to have negligible influence on the calculated reaction free-energies. All calculations of 2H-$MoSe_2$ monolayers were performed using 4 × 4 supercells; periodic boundary conditions (PBCs) were applied within the plane of the monolayer and a vacuum region of 12 Å, obtained from total-energy convergence tests, was inserted normal to the layers. Brillouin zones of these supercells were sampled using 3 × 3 × 1 Γ-centered k-point meshes. Similar to prior studies, [9,59–61] Mo-edges and Se edges were modeled using nanoribbons obtained by applying PBCs along only one of the in-plane directions and retaining four unit cells along the ribbon width. Nanoribbon images were separated from each other by a vacuum regions of 12 Å along the ribbon width and layer normal directions.

The Brillouin zones of these nanoribbons were sampled using 1 × 3 × 1 Γ-centered k-point meshes. The PBE lattice parameter for 2H-$MoSe_2$ monolayer was calculated to be 3.32 Å which is

comparable to the experimentally obtained lattice parameter of 3.29 Å.[62] The TM-doped $MoSe_2$ basal planes, Mo-edges and Se edges were obtained by substituting one Mo atom with a TM dopant atom. Se vacancies (V_{Se}) were produced in basal planes and edges by removing one Se atom from the respective pristine (defect-free) model. The free-energy of H adsorption, ΔG_H, was calculated by adsorbing one H atom on either the basal plane of the monolayer or the edge of the nanoribbon. H-adsorbed structures were relaxed with dipole corrections[63] applied either normal to the monolayer (for basal-plane adsorption) or along the width of the nanoribbons (for adsorption at edges). ΔG_H on Pt(111) surface at low (1/9 monolayer) H-coverage were taken from our previous work.[64]

The zero-point energy, E_{ZPE}, is calculated as $E_{ZPE} = \sum_i \hbar\omega_i/2$, where $\hbar$ is the reduced Planck's constant and ω_i is the vibrational frequency. Here, ω_i is obtained by perturbing the H atom from its equilibrium position by ± 0.015 Å in all three Cartesian directions, and diagonalizing the mass-weighted Hessian matrix; the larger Mo and Se atoms were held fixed due to their much larger masses than H. For ΔG_{DSR} calculations, the vibrational frequencies of the $MoSe_2$ ML, with and without the vacancy, are calculated by displacing the Se atom (vacancy formation site) and its neighboring TM, Mo, and Se atoms (Figure S1) from their equilibrium positions by ± 0.015 Å in all three Cartesian directions, and diagonalizing the mass-weighted Hessian matrix. The vibrational entropy, S_{vib}, may then be estimated as,[65]

$$S_{vib} = k_B \sum_{i=1}^{N} \left[-\ln\left(1 - e^{-\frac{\hbar\omega_i}{k_B T}}\right) + \frac{\hbar\omega_i / k_B T}{e^{\frac{\hbar\omega_i}{k_B T}} - 1} \right] \quad (1)$$

where k_B is Boltzmann's constant, T is the temperature (here, T=300K), ω_i is the vibrational frequency and N is the total number of vibrational modes. For gas-phase H_2 and H_2Se molecules, we used standard entropies from the NIST database. [66]

3. RESULTS AND DISCUSSION

3.1 Doped Basal Planes of 2H-$MoSe_2$

3.1.1 Electronic structure

Previous studies[9,23] have shown that the basal plane of 2H-$MoSe_2$ (or also simply $MoSe_2$, henceforth) is inert towards HER because of the highly unfavorable thermodynamics for H adsorption, which is, in turn, a consequence of this material being a semiconductor lacking electronic states near the Fermi level. Thus, to modify the electronic structure of $MoSe_2$, we replaced the Mo atom in a monolayer (ML) with selected *3d* transition metals (TM) dopants—Mn, Fe, Co, and Ni. These TM-dopants have been studied extensively for doping of MoS_2 catalysts,[67–69] and are a convenient choice for understanding trends in model systems wherein *3d* electrons are progressively added to the monolayer. Specifically, in 2H-$MoSe_2$ the Mo *4d* orbitals are split by the trigonal prismatic crystal field into three sets of energy levels, in ascending order of energy, d_{z^2}, $d_{x^2-y^2,\ xy}$ and $d_{xz,\ yz}$;[70–72] the d_{z^2} band is filled, while the other *d* bands are empty. As we replace an Mo atom with TM dopants—starting with Mn up to Ni—valence electrons are progressively added to the unfilled *d* bands. When these electrons remain unpaired there is an overall non-zero magnetic moment accompanied by symmetry breaking due to the Jahn-Teller effect (Table S1). Similar to Mo, the Mn, Fe, and Co dopant atoms remain sixfold coordinated with net magnetic moments of $+1\mu_B$, $+2\mu_B$ and $+1\mu_B$, respectively, consistent with a +4 oxidation state. The unpaired electrons effectively electron-dope the $MoSe_2$ monolayer and we examine the consequences of such doping on H adsorption below. However, in the Ni-doped case, two Ni-Se bonds are broken, and the Ni atom is only fourfold coordinated to Se possessing a net magnetic moment of $+2\mu_B$ consistent with a +2 oxidation state. As shown later, this bond-breaking has

important implications for favorable H adsorption and Se vacancy formation in the neighborhood of Ni dopants.

3.1.2 Hydrogen Adsorption on Defect-Free Basal Planes

The effect of TM dopants on the HER activity of $MoSe_2$ basal planes was examined by calculating the change in free energy for H adsorption, ΔG_H, defined as

$$\Delta G_H = E_{ML+H} - E_{ML} - \frac{E_{H_{2,(g)}}}{2} + \Delta E_{ZPE} - T\Delta S \quad (2)$$

where E_{ML+H}, E_{ML}, and $E_{H_{2,(g)}}$ are the 0 K DFT energies of the $MoSe_2$ monolayer (ML) with a single adsorbed H atom, the pristine ML, and a hydrogen (H_2) molecule in the gas-phase respectively; ΔE_{ZPE} is the difference of zero-point energies of the H atom in its adsorbed and reference state [$\frac{1}{2}H_{2\,(g)}$]; ΔS is the difference between the vibrational entropy of an adsorbed H atom and the standard entropy of H atom in the gas phase, which is approximated as $\approx \frac{1}{2}S^{\circ}_{H_2}$, where $S^{\circ}_{H_2}$ is the standard entropy of gas-phase H_2 molecule at standard conditions. ΔE_{ZPE} and $-T\Delta S$ (at T=300K) are calculated to be 0.06 eV and 0.19 eV, respectively, at the basal plane and edge sites of undoped $MoSe_2$ ML, and we take these values of ΔE_{ZPE} and $-T\Delta S$ to be representative for all doped $MoSe_2$ MLs. ΔG_H is a well-established descriptor of HER activity in acidic media,[73,74] and according to the Sabatier principle,[75] $\Delta G_H \approx 0$ signifies ideal HER thermodynamics[76] such that the strength of hydrogen adsorption is neither too strong nor too weak for hydrogen evolution in the low overpotential range. Negative/positive values of ΔG_H imply over-/under-binding of H atoms to the catalyst surface, leading to non-optimal HER activity. For all cases studied here, we find that Se atoms are the most favorable sites for basal-plane H adsorption [Figure 1(a)] and hence, we only report ΔG_H for these on-top adsorption sites. Figure 1 (b) displays ΔG_H (at 300K) from which we see that H adsorption on the undoped basal plane of $MoSe_2$ is highly unfavorable (ΔG_H

≈ +2 eV). Upon TM doping, H adsorption becomes thermodynamically more favorable at nearest-neighbor Se on-top sites (Figure 1), with ΔG_H decreasing monotonically from Mn- to Ni-doped cases. In the case of Mn, Fe, and Co, the decrease in ΔG_H is significant (0.9 eV, 1.25 eV, and 1.75 eV, respectively) but the resulting adsorption energies are still much too unfavorable ($\Delta G_H >> 0$) to initiate HER at low overpotentials. In contrast, for the Ni-doped case, H adsorption becomes thermodynamically favorable ($\Delta G_H = -0.23$ eV). This stronger binding of H on Ni-doped $MoSe_2$ basal planes occurs due to the presence of undercoordinated Se atoms (two broken Ni-Se bonds) adjacent to the dopant site, as noted previously. It is noteworthy that ΔG_H for the Ni-doped basal plane is comparable to that for the Pt(111) surface ($\Delta G_H = -0.27$ eV) at low H-coverage of 1/9 monolayer, indicating that Ni-doped $MoSe_2$ is a potentially useful HER catalyst. It should be noted though that substituting Mo with Ni is sufficiently endothermic (Table S2) that the occurrence of such Ni-doped basal sites will be small.

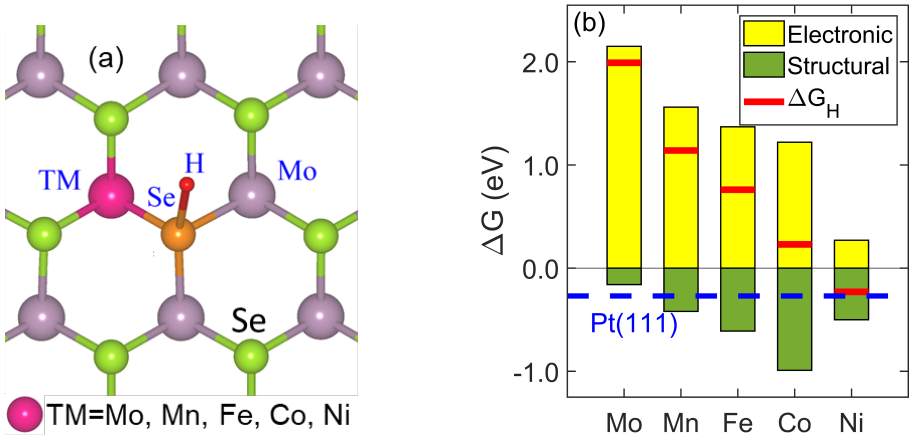

Figure 1. (a) Schematic of $MoSe_2$ basal plane with hydrogen (shown by red sphere) adsorbed on a Se atom (shown by orange sphere). Violet, green, pink, and red spheres represent Mo, Se, TM, and H atoms, respectively. (b) Free-energy change of H adsorption (ΔG_H) on undoped (Mo) and TM-doped $MoSe_2$ basal planes. Yellow and green bars show approximate contribution from electronic interactions between H and $MoSe_2$ ML ($\Delta G_{Electronic}$) and structural relaxation ($\Delta G_{Structural}$) reflected in ΔG_H ($\Delta G_H = \Delta G_{Electronic} + \Delta G_{Structural}$). The blue dashed line indicates ΔG_H for the Pt(111) surface at low H-coverage of 1/9 monolayer.

During H adsorption on the basal plane, two processes, namely, bond formation between H and Se and structural relaxation of the atoms within the $MoSe_2$ layer occur simultaneously. It is instructive to isolate these two events, at least approximately, and calculate their respective contributions to ΔG_H, (*i.e.* $\Delta G_H = \Delta G_{Electronic} + \Delta G_{Structural}$) by performing DFT simulations of H adsorption in two steps. In step 1, $\Delta G_{Electronic}$ is calculated using Eq. 2 but only the H atom is allowed to relax. Since the $MoSe_2$ layer is frozen, $\Delta G_{Electronic}$ approximately captures the free-energy change due to electronic interactions between the Se on-top site and the H atom. In step 2, we allow for complete relaxation of the structure and calculate the free-energy change $\Delta G_{Structural}$ as the difference in energies of the composite structure ($MoSe_2$+H) between steps 1 and 2. The outcome of these calculations is displayed in Figure 1(b) from which we immediately see that the electronic contribution towards H adsorption is generally thermodynamically unfavorable because of positive values of $\Delta G_{Electronic}$; nevertheless, there is a clear trend wherein $\Delta G_{Electronic}$ decreases with electron doping indicating the benefit of substitutional doping with electron-rich dopants. On the other hand, structural relaxation is beneficial for H adsorption and $\Delta G_{Structural}$ decreases monotonically from Mn to Co reflecting a combined effect of atomic size mismatch between Mo and the TM dopant atoms as well as symmetry breaking (Jahn-Teller effect). However, the Ni-doped case deviates from this decreasing trend and this deviation can be rationalized by the entirely different structure that arises from the Ni-Se bond breaking that leaves behind an undercoordinated Se atom, as discussed earlier. Interestingly, in the Ni-doped case, $\Delta G_{Structural}$ is sufficiently negative relative to $\Delta G_{Electronic}$, to render the overall H-adsorption process thermodynamically favorable. Overall, from these results, we see that the selected TM dopants promote favorable H-Se electronic interaction and also increase structural stabilization during the H-adsorption process to improve the overall thermodynamics of H adsorption.

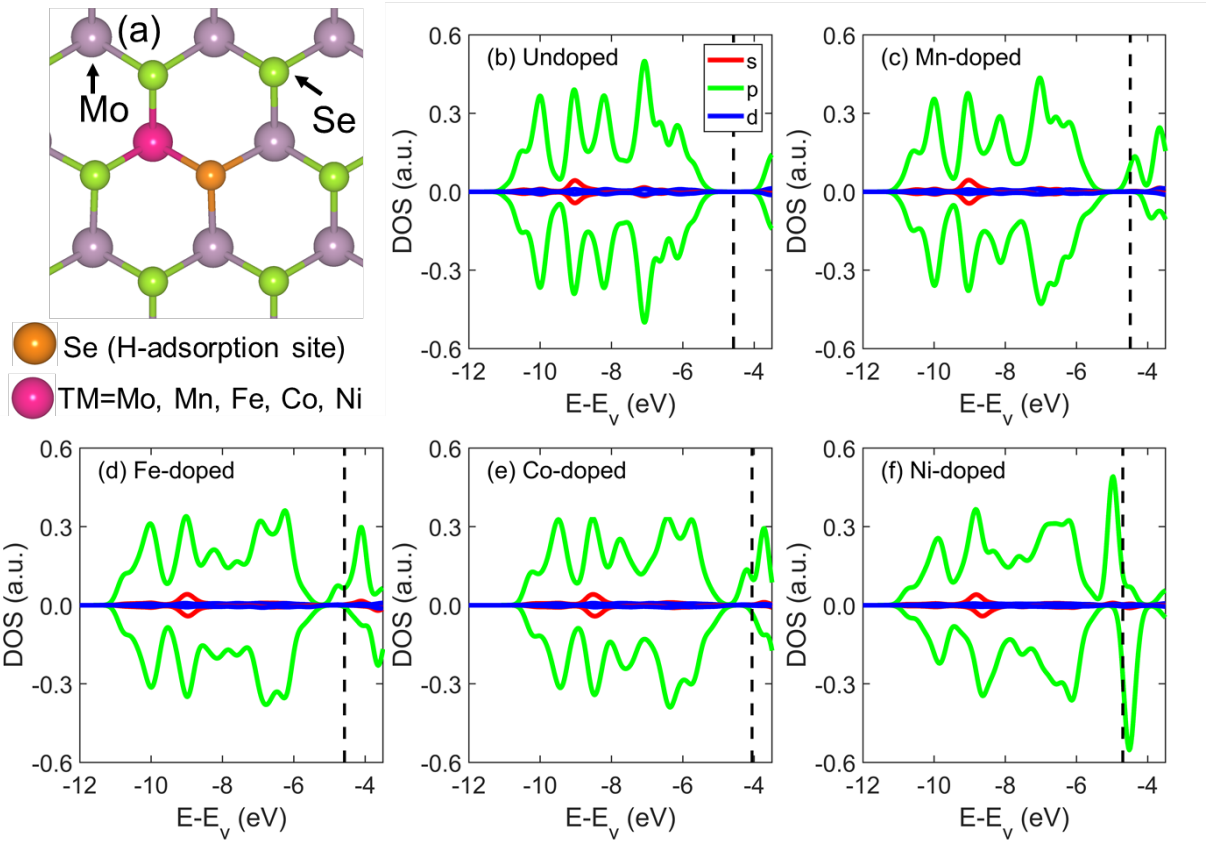

Figure 2. (a) Schematic of $MoSe_2$ basal plane. The TM dopant and its nearest neighbor Se site (H-adsorption site) are shown by pink and orange spheres, respectively. Angular-momentum-projected density of states (DOS) of the H-adsorption site (Se on-top site) on (b) undoped, (c) Mn-doped, (d) Fe-doped, (e) Co-doped, and (f) Ni-doped basal planes; red, green, and blue solid lines represent DOS of s, p and d bands, respectively, of the Se on-top adsorption site; vertical black dashed lines indicate the Fermi level. For consistency, all energies are reported relative to the vacuum level.

To understand further the electronic interactions between the $MoSe_2$ basal plane and hydrogen, we investigated the electronic structure of the Se atom that serves as the H-adsorption site in a defect-free basal plane (Figure 2). In the absence of dopants, the 2H-$MoSe_2$ monolayer is semiconducting and there are no states in the vicinity of the Fermi level to enable favorable bonding with H atoms [Figure 2(b)]. With the introduction of TM dopants [Figures 2(c)-(f)], we notice the emergence of partially-filled Se *p*-states at the Fermi level, rendering the adsorption site metallic in nature. In particular, with increasing *d*-electron count of TM dopants, the density of these partially-filled

states at the Fermi level increases, explaining the observed energetic trend of more favorable H-Se electronic interactions in going from Mn to Ni. The stronger H-Se interactions in the doped cases are also reflected in the electronic structures of the doped MLs with adsorbed H (Figure S2), wherein we observe a monotonic shift of the H-Se bonding states to lower energies with increasing *d*-electron count of the dopant.

Overall, we conclude from these studies that, while substitution of Mo can, in principle, be used to tailor the HER activity of neighboring Se atoms, the effects are still insufficient to achieve activation of the pristine basal plane with the sole exception of Ni doping.

3.1.3 Se Vacancy Formation in Basal Planes

It is well known that chalcogen vacancies are ubiquitous in layered dichalcogenides and are often the most active sites for HER.[22–27] Thus, we must also consider H adsorption at Se vacancies (V_{Se}) to draw any firm conclusions regarding the influence of TM dopants on basal plane activity. Thus, we examine now the thermodynamics of electrochemical vacancy formation in doped $MoSe_2$ monolayers, after which we report H adsorption energies at V_{Se} sites. Chalcogen vacancy defects are created in TMDs during synthesis and can also be generated post-synthesis by methods like ion/electron irradiation, annealing or plasma treatment.[77,78] A recent study by Tsai *et al*.[22] suggested an electrochemical route for the generation of chalcogen vacancies in TMDs, wherein sulfur vacancies in MoS_2 can be generated by increasing the applied cathodic potentials during HER. In a similar manner, Se vacancies in $MoSe_2$ can be generated via electrochemical deselenization, the overall reaction for which is

$$^{*}Se + 2(H^{+} + e^{-}) \rightarrow H_2Se_{(g)} + {}^{*}, \qquad (3)$$

where ***Se* is the reacting Se atom on the $MoSe_2$ surface, (H^+ + e^-) is a proton-electron pair transferred to the catalyst, and * is the resulting Se vacancy (V_{Se}) created in the $MoSe_2$ surface. In

the electrochemical deselenization reaction (DSR) reaction, two (H^+ + e^-) pairs are transferred sequentially as

$$^*Se + (H^+ + e^-) \rightarrow {}^*SeH \quad (4)$$

$$^*SeH + (H^+ + e^-) \rightarrow H_2Se_{(g)} + {}^*. \quad (5)$$

Note that the first step of DSR (Eq. 4) is also the Volmer step of HER, which implies that both DSR and HER will compete on $MoSe_2$ to generate $H_2Se_{(g)}$ and $H_{2,(g)}$, respectively. The reaction free-energy for DSR (Eq. 3), ΔG_{DSR}, is calculated as

$$\Delta G_{DSR} = E_{ML+V_{Se}} + E_{H_2Se,(g)} - E_{ML} - E_{H_{2,(g)}} + \Delta E_{ZPE} - T\Delta S, \quad (6)$$

$$\Delta E_{ZPE} = E_{ZPE,ML+V_{Se}} + E_{ZPE,H_2Se(g)} - E_{ZPE,ML} - E_{ZPE,H_2(g)}, \quad (7)$$

$$\Delta S = S_{vib,ML+V_{Se}} + S^{\circ}_{H_2Se(g)} - S_{vib,ML} - S^{\circ}_{H_{2(g)}}, \quad (8)$$

where $E_{ML+V_{Se}}$, E_{ML}, $E_{H_2Se,(g)}$ and $E_{H_{2,(g)}}$ are the 0 K DFT energies of an $MoSe_2$ ML (doped or pristine) with one Se vacancy, the defect-free ML (doped or pristine), an H_2Se gas molecule, and an H_2 gas molecule, respectively; ΔE_{ZPE} and ΔS are the differences between zero-point energies (E_{ZPE}) and entropies of products [ML+V_{Se} and $H_2Se_{(g)}$] and reactants [ML and $H_{2(g)}$], respectively; $S_{vib,ML+V_{Se}}$ and $S_{vib,ML}$ are the vibrational entropies of $MoSe_2$ ML with and without one Se vacancy, respectively. $S^{\circ}_{H_2Se(g)}$ and $S^{\circ}_{H_{2(g)}}$ are the standard entropies of gas-phase H_2Se and H_2, respectively;[66] T is the temperature (here, T=300 K). We focus on Se vacancy formation at the nearest-neighbor sites of the TM dopant, which we can expect to be maximally perturbed by the introduction of the dopant atom.[33] At the basal plane, both HER and DSR occur at the same Se top site [Figure 3(a)]. Figure 3(b) displays ΔG_{DSR} for undoped and TM-doped $MoSe_2$, from which we see that the energy for Se vacancy formation is highest in the undoped monolayer and progressively decreases from Mn- to Ni-doped cases. Nevertheless, ΔG_{DSR} is sufficiently positive

in all cases implying that moderate to large cathodic potentials are required to initiate vacancy formation (Table 1), even though the decrease in ΔG_{DSR} from the undoped to the Ni-doped case is quite significant (~1.8 eV).

Table 1. Limiting (cathodic) potentials (vs. RHE) for HER ($U_{L,\,HER}$) and DSR ($U_{L,\,DSR}$) on basal planes, Se edges, and Mo edges of undoped and TM-doped $MoSe_2$; dashes indicate that H adsorption or DSR are thermodynamically favorable at standard conditions.

	$U_{L,\,HER}$ (V)			**$U_{L,\,DSR}$ (V)**		
TM Dopant	*Basal plane*	*Se edge* θ_{Se}=1.0	*Mo edge* θ_{Se}=0.5	*Basal plane*	*Se edge* θ_{Se}=1.0	*Mo edge* θ_{Se}=0.5
Undoped	-1.99	-	-	-1.30	-0.34	-0.56
Mn	-1.06	-0.05	-0.27	-0.92	-0.12	-0.38
Fe	-0.76	-	-0.28	-0.77	-0.17	-0.45
Co	-0.23	-0.06	-0.27	-0.55	-0.16	-0.36
Ni	-	-0.13	-0.07	-0.39	-0.09	-0.23

Table 2. Relative change in TM-Se ($\Delta d_{TM\text{-}Se}/d_{TM\text{-}Se}$) and nearest-neighbor Mo-Se ($\Delta d_{Mo\text{-}Se}/d_{Mo\text{-}Se}$) bond lengths upon H adsorption at a Se atom in the basal plane; $d_{Se\text{-}H}$ is the distance between the Se atom (adsorption site) and adsorbed H atom [see Figure 3(a) for labeling of bonds]

TM Dopant	**$\Delta d_{TM\text{-}Se}/d_{TM\text{-}Se}$ (%)**	**$\Delta d_{Mo\text{-}Se}/d_{Mo\text{-}Se}$ (%)**	**$d_{Se\text{-}H}$ (Å)**
Undoped	+10.63	+0.39	1.57
Mn	+23.77	+2.75	1.54
Fe	+29.22	+3.14	1.52
Co	+33.47	+3.14	1.51
Ni	+34.27	+2.75	1.51

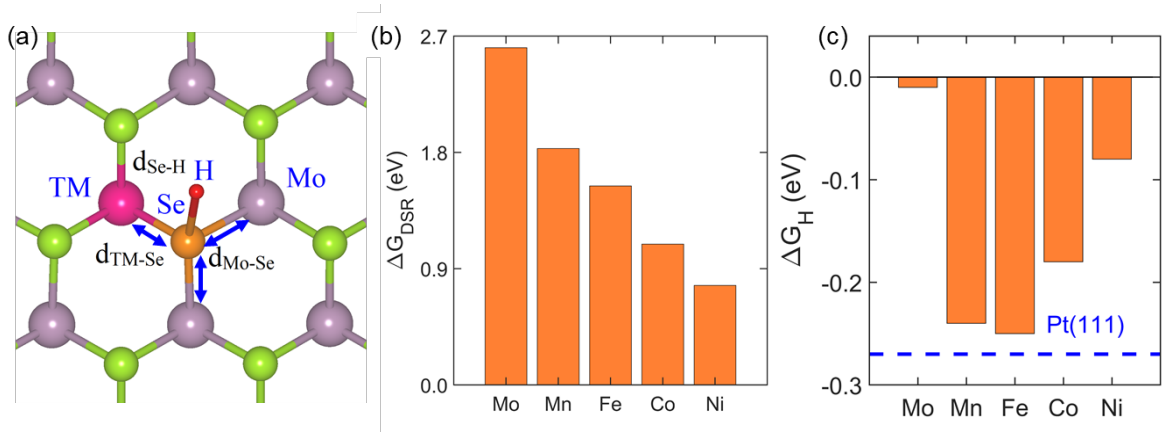

Figure 3. (a) Schematic of defect-free $MoSe_2$ basal plane with H adsorbed at an Se on-top site (represented by orange sphere); d_{Se-H}, d_{TM-Se}, and d_{Mo-Se} are bond lengths between indicated Se-H, TM-Se, and Mo-Se atoms, respectively, after H-adsorption. (b) Reaction free-energy for DSR (ΔG_{DSR}) at undoped (Mo) and TM-doped $MoSe_2$ basal planes. (c) ΔG_H at V_{Se} site on undoped (Mo) and TM-doped $MoSe_2$ basal planes. V_{Se} site is created by the removal of one Se atom (H-adsorption site represented by orange sphere) from the basal plane. The blue dashed line represents ΔG_H for the Pt(111) surface at low (1/9 monolayer) H-coverage.

The trends in ΔG_{DSR} for the basal plane can be understood by examining jointly the electronic structure of the Se site for H adsorption in the Volmer step (Equation 4) and local structural changes caused by this H-adsorption event. As noted previously, TM doping of $MoSe_2$ leads to the emergence of half-filled *p* states at Se nearest neighbors of the dopant atom. These Se *p* states are higher in energy than those in undoped $MoSe_2$, which is indicative of electronic destabilization of the Se neighbors by the TM dopants; this destabilizing effect is amplified from Mn to Ni, as discussed before. Upon H adsorption at these Se on-top sites, there is a significant change in local structure that can be quantified by examining the Mo-Se and TM-Se bond lengths [Figure 3(a) and Table 2]. Specifically, we see from Table 2 that the TM-Se and Mo-Se bonds are elongated (weakening of bonds) around the adsorption site. In the undoped case, H adsorption breaks C_{3v} symmetry with one Mo-Se bond elongating by ~11% (Table 2). For the doped cases, the elongation in TM-Se bond length is even more substantial, increasing monotonically from Mn (~24%) to Ni

(~34%); the Mo-Se bond elongation is comparatively smaller but still non-negligible (~3% elongation). The Se-H bond, on the other hand, shortens upon the introduction of a TM dopant, ranging from ~2% for Mn to ~4% for Ni. Collectively, these observations indicate that (a) H adsorption weakens the Mo-Se and TM-Se bonds, which is then conducive to vacancy formation (via DSR), and (b) destabilization of the Se on-top site is more pronounced with increasing *d*-electron count of the dopant atom, making vacancy formation more energetically feasible.

3.1.4 H Adsorption at Se Vacancy Sites

To complete the analysis of pristine vs. doped basal planes, we finally examine H adsorption at the V_{Se} sites. As seen from the data in Figure 3(c), $\Delta G_H \approx 0$ only for V_{Se} sites in the undoped basal plane. V_{Se} sites in Ni-doped $MoSe_2$ bind H slightly more strongly, although with small $\Delta G_H \approx$ -0.07 eV. However, for Mn-, Fe- and Co-doped $MoSe_2$, H tends to overbind at V_{Se} sites ($\Delta G_H \sim$ -0.20 eV); nevertheless, these V_{Se} sites might still be expected to be active for HER given that their ΔG_H values are comparable to the active Pt (111) surface, i.e., with the consideration of kinetics, the required overpotential could push cathodic potentials towards 0 V.

3.1.5 Effect of TM Dopants on HER vs. DSR Thermodynamics

As HER and DSR can compete for active sites on the basal plane, it is important to understand the impact of TM dopants on the thermodynamics of the two competing reactions. Accordingly, we employed the Computational Hydrogen Electrode (CHE)[79] model to calculate the limiting potential (U_L), relative to the reversible hydrogen electrode (RHE), required to render HER and DSR exergonic (Figure S3). The reaction Gibbs free-energy, ΔG, at an applied electrode potential, U_L, is calculated as[79]

$$\Delta G = \Delta E + \Delta E_{ZPE} - T\Delta S - n\, e^{-}\, U_L, \quad (9)$$

where ΔE is the DFT reaction energy at 0 K, ΔE_{ZPE} is the difference of zero-point energies of products and reactants, ΔS is the change in entropy for the reaction step at standard temperature (T = 300 K), n is the number of (H^++e^-) pairs transferred in the reaction step, and U_L is the limiting electrode potential (relative to RHE) required to render the reaction exergonic (ΔG=0). U_L is only reported here when the reaction is thermodynamically unfavorable at standard conditions, *i.e.*, when $\Delta G° = (\Delta E+\Delta E_{ZPE}-T\Delta S) > 0$; for HER: $\Delta G° = \Delta G_H$, and DSR: $\Delta G° = \Delta G_{DSR}$. On the catalyst surface, HER and DSR occur after the transfer of one and two successive (H^+ + e^-) pairs, respectively. At low overpotentials ($U_L \sim 0$ V) with the exception of the Ni-doped case, both HER and DSR are thermodynamically uphill regardless of the choice of TM dopant, HER being more favorable than DSR. For the Ni-doped case, only DSR is thermodynamically uphill in energy while HER has negative free-energy, which indicates that H adsorption is spontaneous. Upon increasing the cathodic potential (Figure S3 and Table 1) DSR becomes exergonic before HER at lower U_L for undoped and Mn-doped $MoSe_2$; for the Fe-doped case, both HER and DSR occur at nearly the same U_L whereas, for the Co-doped case, the onset of HER occurs before DSR. While the details of the onset of HER vs. DSR are sensitive to the choice of TM dopant, in all TM-doped cases we note that the limiting potentials required for both HER and DSR are lower than that for the undoped basal plane case. This is consistent with prior experiments that report lower overpotentials for HER on TM-doped $MoSe_2$ catalysts;[33,46] we are not aware of similar reports for DSR but our predictions can be verified using procedures similar to those reported in the literature.[22,52,53]

3.2 Doped Edges of 2H-$MoSe_2$

Edges of TMDs are well known to be highly active for HER[8–16] and prior studies on $MoSe_2$,[11,12] specifically, have shown that the HER activity can be improved by exposing more edges sites. Thus, we sought to understand the role of TM dopants at the edges of $MoSe_2$ and, for this purpose, we considered two well-studied edge terminations, namely, the Se edge with 100% Se-coverage (θ_{Se}=1.0) and the Mo-edge with 50% Se-coverage (θ_{Se}=0.5). The Mo edge with 100% Se-coverage was excluded because 100% Se-coverage was found to be thermodynamically less stable than 50% Se coverage (Figure S4). The Se coverage (θ_{Se}) at an edge is calculated as, $\theta_{Se} = n_{Se}/(2 \times n_{Mo})$, where n_{Se} and n_{Mo} are the number of Se and Mo atoms at the edge, respectively.

3.2.1 Se edge (θ_{Se}=1.0)

Structure of Doped Edges

Similar to the basal plane, at the Se edge (θ_{Se}=1.0) Mo atoms are sixfold coordinated to Se. Along this edge, we also observe that every other pair of Se atoms tends to dimerize and this reconstruction is well known from previous studies.[9,80] After TM doping, clear distortions in the local edge structure are observed due to the smaller size of the TM dopants relative to the Mo atom (Table S3). Specifically, in all TM-doped cases, the TM-atom–Se bonds are shorter than Mo–Se bond: in Mn- and Fe-doped cases, the TM dopant nevertheless remains sixfold coordinated; however, for Co- and Ni-doped cases, the dopant atoms are only fivefold coordinated while the sixth Se atom is repelled by dopant and forms a stronger bond with adjacent Mo and Se atoms (Figure S5 and Table S3).

Hydrogen Adsorption at Defect-Free Edges

Figure 4(g) displays ΔG_H at undoped and doped Se edges (θ_{Se}=1.0). The Se edge of undoped $MoSe_2$ optimally binds the adsorbed H atom ($\Delta G_H \approx 0.00$ eV); with Fe-doping too, ΔG_H is negligibly small (~ 1 meV) indicative of nearly optimal binding of H for HER. For the remaining dopants, H is slightly under bound at the edges, with ΔG_H of about 50, 60, and 130 meV for Mn, Co, and Ni, respectively. Nevertheless, these adsorption energies are much smaller (less positive) than those on the basal plane suggesting that HER can be initiated at much lower cathodic potentials.

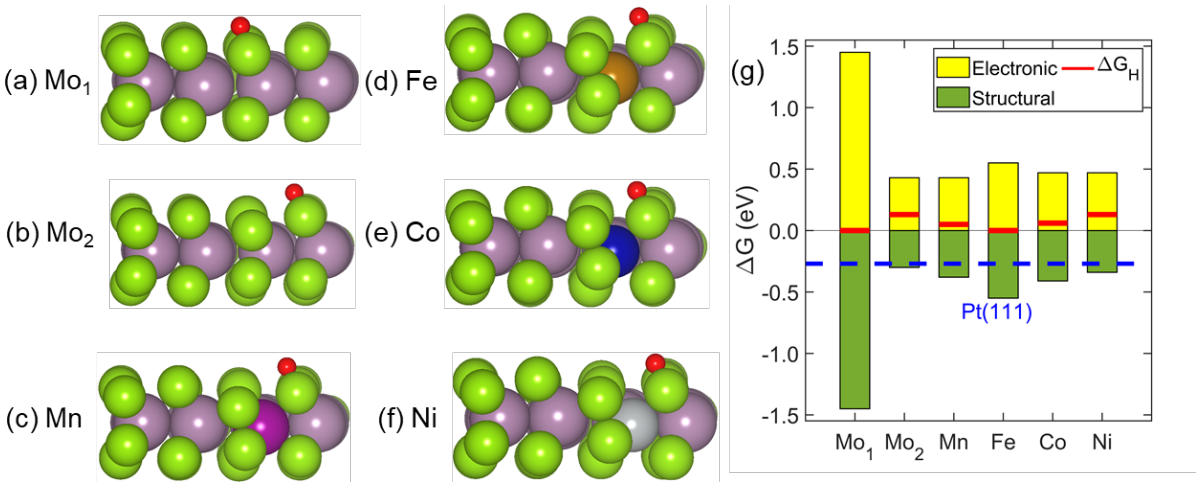

Figure 4. Side view of the relaxed structures of Se edges (θ_{Se}=1.0): (a, b) H adsorption at a dimerized Se atom (Mo_1) and a non-dimerized Se atom (Mo_2) on the undoped Se edge, the Mo_1 case being energetically preferred; (c)-(f) TM-doped Se edges with H adsorbed at the (most favorable) non-dimerized Se sites. (g) Free-energy change of H adsorption (ΔG_H) at undoped (Mo) and TM-doped Se edges: yellow and green bars show approximate contribution of electronic interactions between H and the $MoSe_2$ ML ($\Delta G_{Electronic}$) and structural relaxation ($\Delta G_{Structural}$) towards the free-energy of H adsorption ($\Delta G_H = \Delta G_{Electronic} + \Delta G_{Structural}$). The blue dashed line indicates ΔG_H for the Pt(111) surface at low (1/9 monolayer) H-coverage. Violet, green, pink, golden, blue, grey, and red spheres represent Mo, Se, Mn, Fe, Co, Ni and H atoms, respectively.

From the structural models in Figures 4(a-f) and Figure S6, we note that the most favorable H-adsorption site on undoped and TM-doped Se edges are different and, moreover, the large structural distortions at Se edges render these sites rather dissimilar (Table S3). In particular, when we examined H adsorption on the undoped edge at a non-dimerized Se atom, [Figure 4(b), and

Figure S6] which is the favored adsorption sites on a doped edge, we found this site to be less stable for H adsorption (ΔG_H = +0.13 eV, Mo_2) than a dimerized Se site (ΔG_H = 0.0 eV, Mo_1). This is somewhat counterintuitive as H adsorption could be expected to be stronger at the non-dimerized Se atom, which is undercoordinated relative to the dimerized one. However, structural distortions upon H adsorption turn, as quantified by $\Delta G_{Structural}$ in Figure 4(g), out to be sufficiently important such that breaking an Se dimer is less energetically expensive than destabilizing metal-Se bonds. Similar observations were also reported by Nørskov and coworkers[9,80] for S/Se edges of MoS_2 and WSe_2 monolayers. We also note that variations in ΔG_H between the various doped edges are small (~ 50-130 meV) and there are no clear trends in ΔG_H after TM-doping. In general, at the Se edge, we see that TM dopants have a small destabilizing effect on H adsorption, which is determined by the complex interplay of electronic interactions and structural relaxation. On comparing $\Delta G_{Electronic}$ and $\Delta G_{Structural}$ for H adsorption at a non-dimerized Se atom, we find that TM dopants have negligible influence on electronic interactions between the Se edge and H: $\Delta G_{Electronic}$ remains nearly unchanged between 0.43 eV to 0.47 eV after TM doping, except for the Fe-doped case for which $\Delta G_{Electronic}$ = +0.55 eV. $\Delta G_{Structural}$, on the other hand, varies between -0.55 eV to -0.34 eV after doping but is, in general, insufficient to overcome larger $\Delta G_{Electronic}$. We further investigated the electronic structures and local geometries of the Se edges and found that, after TM doping, Se atoms (non-dimerized Se adsorption sites) have fairly similar electronic structures [Figure S7 (b)-(f)], which explains the nearly constant $\Delta G_{Electronic}$ in Figure 4(g). The local structural changes caused by the TM dopants can explain the slight destabilization of H adsorption (see d_{TM-B} in Table S3), as metal-Se and Se-Se bonds near the dopant site become shorter—and thus stronger—rendering the Se atoms near the dopant site less suitable for H adsorption (*i.e.*, slightly more positive ΔG_H).

Se vacancy Formation at Edges

At undoped and TM-doped Se edges, Se vacancy formation (via DSR) is always found to be most favorable at a non-dimerized Se atom (Figure S6). Following a similar approach as for the basal plane, we calculated ΔG_{DSR} for removal of a non-dimerized Se atom from the Se edge and, as seen from Figure 5(b), the effect of TM doping is significant. In particular, ΔG_{DSR} decreases from nearly 0.68 eV for the undoped Se edge to less than 0.34 eV for TM-doped Se edges. Also, these DSR energies—essentially, vacancy formation energies, up to an additive constant—are much smaller than those for the basal plane for which the smallest ΔG_{DSR} (Ni-doped case) was ~ 0.77 eV. Thus, we may expect a higher probability of inducing Se vacancies at the Se edge than in the basal plane for all TM dopants considered here.

To understand trends in DSR energetics, we focus on structural distortions caused by H adsorption (Volmer step) during DSR; the electronic structures of the non-dimerized Se-atoms (H-adsorption sites) are less useful for our present purposes, being rather similar as noted previously. For undoped Se edges, Mo-Se bond lengths are elongated after H adsorption (Table 3), which implies that the Se atom is weakly attached to the Se edge after H adsorption. Upon introducing a TM dopant, H adsorption at a nearest-neighbor Se site is also accompanied by ~6-8% elongation of the Mo-Se bond while the TM-Se bond remains mostly unaffected [Table 3; Figure 5(a)]. This weakening of the Mo-Se bond makes it easier for Se vacancies to be generated upon attack by a second proton and the trends in Mo-Se bond elongation are indeed directly correlated with the calculated ΔG_{DSR} [Table 3; Figure 5(b)].

Hydrogen Adsorption at Se Vacancies

Contrary to the defect-free Se edge, the impact of TM doping on H adsorption at a Se vacancy (V_{Se}) is found to be substantial [Figure 5(c)]. First, we note that $\Delta G_H = +0.04$ eV at a V_{Se} site on

undoped Se edge, which is again indicative of slight under-binding of H, unlike the defect-free edge. After TM doping though, H binding at this V_{Se} site is stronger: in all TM-doped cases, ΔG_H becomes more negative and varies between -0.15 eV and -0.21 eV. In short, TM doping will make the V_{Se} site at a Se edge more favorable for HER. Thus, in conjunction with the fact that Se vacancies at edges are more readily formed upon TM doping, we conclude that TM-doping at Se edges could indeed boost HER activity.

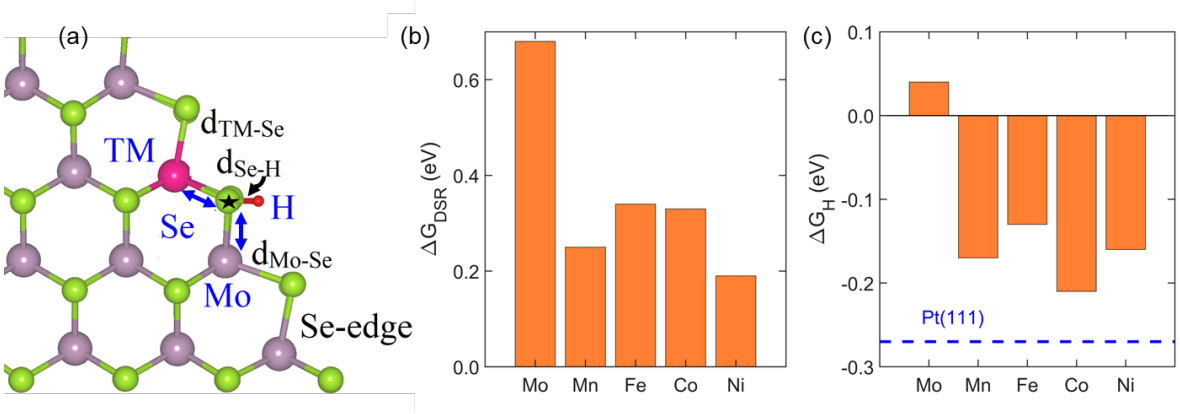

Figure 5. (a) Top view of the Se edge (θ_{Se}=1.0) indicating bond lengths between Mo-Se, TM-Se and Se-H atoms (d_{Mo-Se}, d_{TM-Se}, and d_{Se-H}, respectively); a Se vacancy (V_{Se}) is created by the removal of one non-dimerized Se atom at the Se edge, marked by a black star. (b) ΔG_{DSR} at undoped and TM-doped Se edges. (c) ΔG_H at V_{Se} site on undoped and TM-doped $MoSe_2$ Se edge. The blue dashed line indicates ΔG_H for Pt(111) at low (1/9 monolayer) H-coverage.

Table 3. Relative change in TM-Se ($\Delta d_{TM\text{-}Se}/d_{TM\text{-}Se}$) and nearest-neighbor Mo-Se ($\Delta d_{Mo\text{-}Se}/d_{Mo\text{-}Se}$) bond lengths upon H adsorption at a non-dimerized Se atom along the Se edge; $d_{Se\text{-}H}$ is the distance between the Se atom (adsorption site) and adsorbed H atom [see Figure 5(a) for labeling of bonds] at Se edge.

TM Dopant	$\Delta d_{TM\text{-}Se}/d_{TM\text{-}Se}$ (%)	$\Delta d_{Mo\text{-}Se}/d_{Mo\text{-}Se}$ (%)	$d_{Se—H}$ (Å)
Mo (Undoped)	+2.38	+5.26	1.50
Mn	+0.41	+6.91	1.51
Fe	-0.83	+6.94	1.51
Co	-0.42	+8.20	1.51
Ni	+0.00	+7.41	1.50

HER vs. DSR Thermodynamics

On undoped Se edges, H adsorption is already thermodynamically neutral at zero applied voltage whereas DSR is uphill in energy [Figure S8 (a)] requiring a limiting potential of about -0.34 V to become exergonic (Table 1). Thus, it is unlikely that HER and DSR will compete at low cathodic potentials. Upon TM doping of Se edges, ΔG_{DSR} decreases significantly, as noted above, and thus the limiting potential for DSR is also substantially reduced (Table 1). Additionally, the free-energy difference between DSR and HER also decreases significantly [Figure S8 (b)-(e)] and both reactions become competitive at lower limiting potentials with $U_{L,\,DSR}$ and $U_{L,\,HER}$ lying within a window of -50 mV to -170 mV for all dopants considered here (Table 1). Specifically, for the Mn- and Co-doped Se edges, HER become exergonic at smaller limiting potentials of -50 mV and -60 mV, respectively; DSR, on the other hand, need marginally higher limiting potentials of -120 mV and -160 mV on Mn- and Co-doped Se edges, respectively; for Ni-doped Se edge, DSR becomes exergonic at lower limiting potentials than HER; for the Fe-doped Se edge, H adsorption is already thermodynamically neutral at zero applied voltage whereas DSR is uphill in energy and requires a limiting potential of about -170 mV to become exergonic. In short, we expect that these V_{Se} active

sites can be electrochemically induced at fairly low cathodic potentials providing a facile route for further activation of TM-doped $MoSe_2$.

3.2.2 Mo edge (θ_{Se}=0.5)

An earlier study[9] showed that the Mo edge of $MoSe_2$ is more thermodynamically stable at 50% Se coverage (θ_{Se} = 0.5) than at 100% Se-coverage (θ_{Se} = 1.0). We have independently confirmed those results for pristine $MoSe_2$ and also found this partial coverage to be preferred for our TM-doped cases (Figure S4). Thus, we only focus on the θ_{Se} = 0.5 Mo edge for the remainder of this paper.

Structure of Doped Edges

At the undoped Mo edge (θ_{Se}=0.5), each Mo atom is sixfold coordinated to Se (Figure S9). After TM doping, due to the smaller atomic sizes of the selected dopants, the Mo-Se and TM-Se bond lengths decrease (Table S4) and TM-dopant remain sixfold coordinated to Se atoms like other Mo atoms. Unlike Co- and Ni-doped Se edges, no major edge reconstructions are observed at Mo edge due to doping.

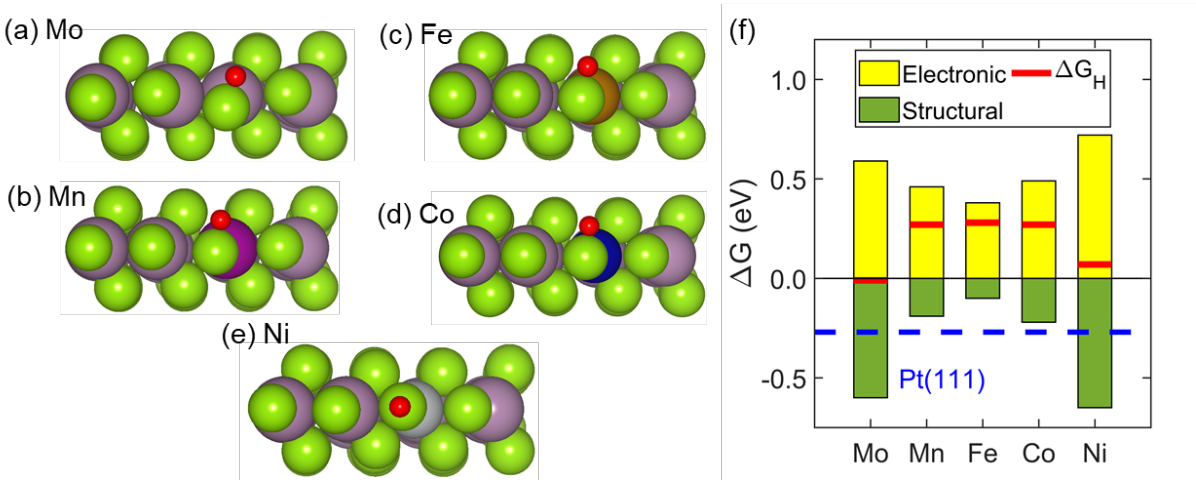

Figure 6. Side views of the relaxed structures of (a) undoped, (b)-(e) TM-doped Mo edges (θ_{Se} = 0.5) with H adsorbed at most favorable adsorption sites. (f) Free-energy change of H adsorption (ΔG_H) at undoped (Mo) and TM-doped Mo edges: yellow and green bars show approximate contribution of electronic interactions between H and $MoSe_2$ ML ($\Delta G_{Electronic}$) and structural relaxation ($\Delta G_{Structural}$) towards the free-energy of H adsorption ΔG_H ($\Delta G_H = \Delta G_{Electronic} + \Delta G_{Structural}$). The blue dashed line indicates ΔG_H for Pt(111) at low (1/9 monolayer) H-coverage. Violet, green, pink, golden, blue, grey, and red spheres represent Mo, Se, Mn, Fe, Co, Ni and H atoms, respectively.

Hydrogen Adsorption at Defect-Free Edges

Figures 6 (a)-(e) and Figure S9 display the most favorable sites for H adsorption at undoped and TM-doped Mo edges. ΔG_H for the undoped Mo edge is -0.01 eV [Figure 6(f)] leading to optimal binding of H for HER. After TM-doping, we find consistent destabilization of H adsorption at the Mo edge. With Mn, Fe and Co doping H-adsorption is significantly destabilized (excessive underbinding; ΔG_H = +0.27 eV), while Ni doping results in small underbinding of H with ΔG_H = +0.07 eV. By decomposing ΔG_H into electronic ($\Delta G_{Electronic}$) and structural ($\Delta G_{Structural}$) contributions [Figure 6 (f)], we find that the electronic contribution is destabilizing for all dopants. The structural contribution, on the other hand, is always stabilizing but insufficient to overcome electronic destabilization in the TM-doped cases.

The unfavorable electronic interactions between the Mo edge (θ_{Se}=0.5) and H atoms upon TM doping can be explained by examining the electronic structure of the H-adsorption sites. From Figure S11 (b)-(f), we see that the density of half-filled *p*-states near the Fermi-level is small for the undoped and Ni-doped Mo edges, which translates into weaker Se-H interactions and more positive $\Delta G_{Electronic}$. On Mn-, Fe- and Co-doped Mo edges, the density of half-filled *p*-states near the Fermi-level is relatively higher than the undoped Mo edge and this results in smaller $\Delta G_{Electronic}$ than the undoped case by at least 0.10 eV. However, less stabilization is achieved from structural relaxation during H-adsorption on Mn-, Fe- and Co-doped Mo edges due to TM-Se bonds being stronger (shorter by ~ 4-6%) than the Mo-Se bond in the undoped Mo edge. (Table S4).

Se vacancy Formation at Edges

The undoped Mo edge (θ_{Se}=0.5) has ΔG_{DSR} of 1.12 eV [Figure 7(b)], which suggests that a large cathodic potential is required for electrochemical creation of a Se vacancy. With TM doping, however, ΔG_{DSR} is significantly reduced in all cases: for Mn-, Co-, and Ni-doped edges, ΔG_{DSR} decreases by 0.36 eV, 0.39 eV, and 0.66 eV, respectively, relative to the undoped edge; for the Fe-doped case, the decrease is more modest (0.22 eV). It is also interesting that, for the Mo edge (unlike the basal plane or Se edges), the active sites for HER and DSR can be different as seen for the Co-doped case (Figure S9). This observation could potentially be of interest for bifunctional effects at Mo edges in more complex reactions.

Table 4. Relative change in TM-Se ($\Delta d_{TM\text{-}Se}/d_{TM\text{-}Se}$) and nearest-neighbor Mo-Se ($\Delta d_{Mo\text{-}Se}/d_{Mo\text{-}Se}$) bond lengths upon H adsorption at a Se atom in the Mo edge (θ_{Se}=0.5); $d_{Se\text{-}H}$ is the distance between the Se atom and an adsorbed H atom [see Figure 7 (a)].

TM Dopant	$\Delta d_{TM\text{-}Se}/d_{TM\text{-}Se}$ **(%)**	$\Delta d_{Mo\text{-}Se}/d_{Mo\text{-}Se}$ **(%)**	$d_{Se—H}$ **(Å)**
Mo (Undoped)	+3.11	+3.88	1.50
Mn	+2.85	+5.12	1.50
Fe	+1.66	+5.12	1.50
Co	+0.00	+5.58	1.50
Ni	+38.71	+2.00	1.50

For rationalizing the trends in ΔG_{DSR} for TM-doped Mo-edges (θ_{Se}=0.5) [Figure 7(b)], we considered the influence of H adsorption on the local structure of the Mo edge and on the stability of metal-Se bonds. As seen from Table 4, H adsorption at Mo edges (θ_{Se}=0.5) causes elongation of both TM-Se and Mo-Se bonds (by several percent) effectively weakening the binding of the Se atom to the edge. For the Mn- and Co-doped cases, the metal-Se bonds are elongated by nearly similar amounts resulting in comparable values of ΔG_{DSR} (~ 0.75 eV). However, for the Fe-doped case, the metal-Se bond elongation upon H adsorption is slightly smaller when compared with other doped cases, and this results in a slightly larger ΔG_{DSR} relative to other doped Mo edges. For the Ni-doped case, the destabilizing effect of the Ni dopant is further amplified upon H adsorption with a large change in the Ni-Se bond length (~38%), which ultimately facilitates a much smaller ΔG_{DSR} of 0.46 eV.

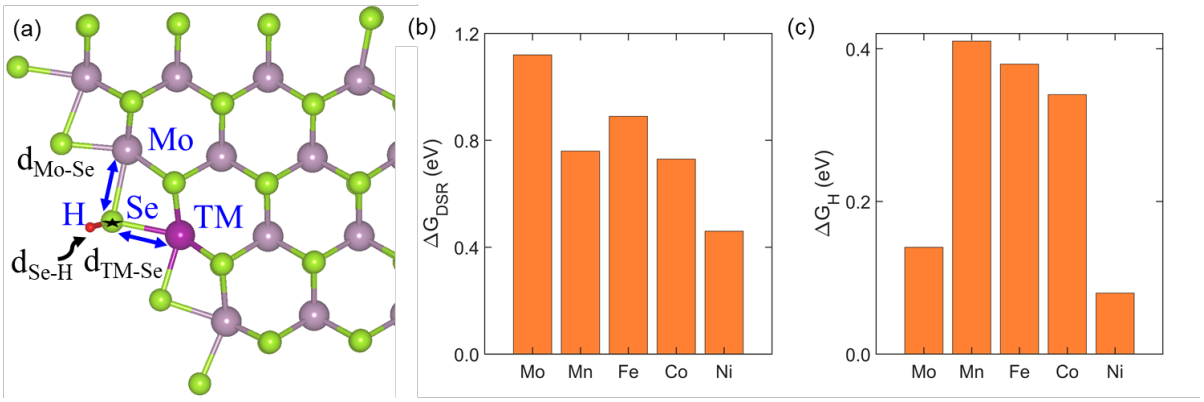

Figure 7. (a) Schematic of Mo edge (θ_{Se}=0.5) indicating bond lengths between Mo-Se, TM-Se and Se-H atoms (d_{Mo-Se}, d_{TM-Se}, and d_{Se-H}, respectively). A Se vacancy (V_{Se}) is created by removal of one Se atom at the Mo edge, marked by a black star. (b) ΔG_{DSR} at undoped and TM-doped Mo edges (θ_{Se}=0.5) (c) ΔG_H at V_{Se} sites in undoped and TM-doped $MoSe_2$ Mo edges (θ_{Se}=0.5).

Hydrogen adsorption at Se Vacancies

Figure 7 (c) displays ΔG_H for H adsorption at V_{Se} sites at the Mo edge (θ_{Se}=0.5); We observe that V_{Se} sites in undoped and Ni-doped Mo edges (θ_{Se}=0.5) have ΔG_H of 0.14 eV and 0.08 eV, respectively, and these V_{Se} sites could potentially be activated at low cathodic potentials. On the other hand, V_{Se} sites in Mn-, Fe- and Co-doped Mo edges (θ_{Se}=0.5) are found to have large and positive $\Delta G_H > +0.35$ eV, indicating that these sites will require larger cathodic potentials and are not particularly desirable for HER.

HER vs. DSR Thermodynamics

On undoped and defect-free Mo edges (θ_{Se}=0.5), H adsorption is already thermodynamically neutral at 0 V; DSR requires a limiting potential of -0.56 V [Figure S12 (a) and Table 1] and HER at the V_{Se} site becomes exergonic at small limiting (cathodic) potentials of -0.14 V. On TM-doped Mo edges, DSR occurs at lower limiting potentials ($U_{L,\ DSR}$), relative to the undoped Mo edge,

lying between -0.23 V to -0.45 V; the limiting cathodic potentials for HER ($U_{L, HER}$) on all doped edges are larger than the undoped Mo edge, with the exception of the Ni-doped Mo edge which requires small $U_{L, HER}$ of -0.07 V. In all doped cases, $U_{L, HER}$ is smaller than $U_{L, DSR}$ by at least 90 mV which indicates that these two processes will likely not compete at low overpotentials.

In summary, unlike the Se edge, V_{Se} sites are less desirable at Mo edges, requiring larger cathodic potentials for HER. However, since the formation of vacancy sites at Mo edges requires larger limiting potentials than at the Se edge (Table 1), it might be possible to work within a potential window wherein active V_{Se} sites can be generated preferentially at the Se edge thereby not compromising the reasonable HER activity of defect-free Mo edges.

4. HER active sites in transition metal doped $MoSe_2$ electrocatalyst

According to the Sabatier principle,[75] an ideal HER catalyst surface binds H neither too strongly nor too weakly for facile hydrogen evolution, and this concept is graphically represented by the so-called volcano plot between the HER activity and the hydrogen binding energy (HBE). The HBE is defined as

$$HBE = E_{ML+H} - E_{ML} - \frac{E_{H_2}}{2}, \quad (10)$$

where E_{ML+H}, E_{ML}, and E_{H_2} are the 0K DFT energies defined previously in Eq. 2; we use the HBE rather than ΔG_H here to compare with similar data from the literature. [73,81] The peak of the volcano corresponds to the maximum HER activity and optimal HBE of an ideal catalyst. For HER in an acidic medium, in particular, Esposito *et al.*[81] have reported that optimal HBE for

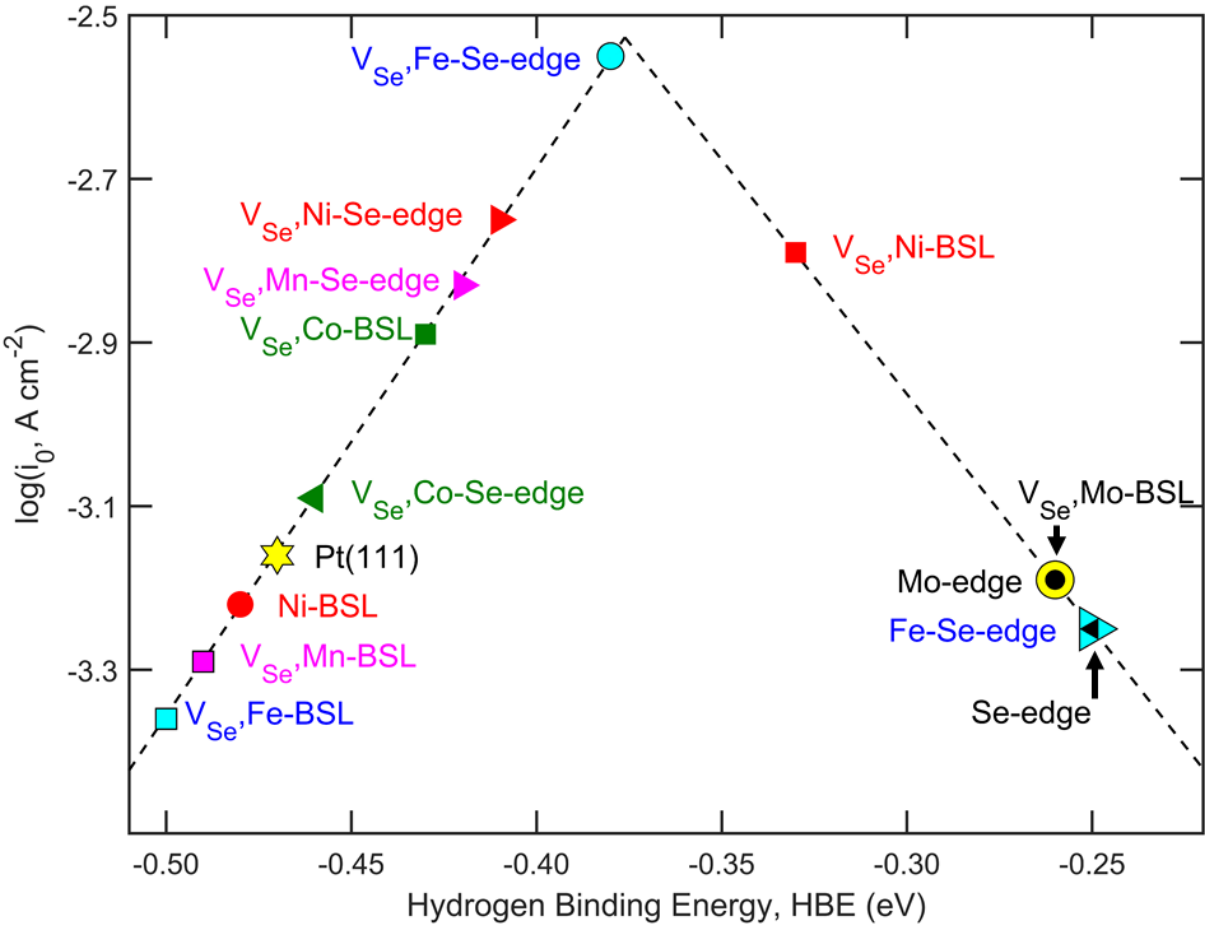

Figure 8. Volcano plot for HER in an acidic medium: the HER exchange current densities [log(i_0)] is plotted against the hydrogen binding energy (HBE). The HER exchange current densities of TM-doped $MoSe_2$ are estimated by superimposing their calculated HBEs over the volcano plot (black dashed lines) of Esposito *et al.*[81] TM-doped basal plane, Mo-edge and Se-edge are abbreviated as TM-BSL, TM-Mo-edge and TM-Se-edge, respectively.

an ideal catalyst surface is -0.37 eV; the Pt(111) surface—an excellent HER catalyst—has HBE of -0.47 eV for low (1/9 monolayer) H-coverage and lies near the peak of the volcano plot. To evaluate, at least approximately, the HER activities of the various active sites studied here, we superimposed our data over the volcano plot that was generated by Esposito *et al.*[81] for various transition metals, transition-metal carbides, and metal overlayer supported on transition-metal-carbides surfaces (black dashed lines in Figure 8). We emphasize that we have not calculated the

HER exchange current densities [log(i_0)] here and are merely extrapolating the potential activity of our studied catalysts by superimposing data points for our calculated HBEs over the volcano plot. Specifically, we have not included the effects of reaction kinetics on HER activity and are solely using thermodynamic descriptor (HBE) to estimate HER activities of various $MoSe_2$ sites from a thermodynamic volcano plot (Figure 8). In practice both reaction thermodynamics and kinetics are important in determining the HER activity of a catalyst; indeed, for HER on TMDs like $MoSe_2$ and MoS_2, both reaction kinetics and thermodynamics are known to have a significant influence on HER activity.[25,82–84] Also, our calculated HBE for Pt (111) with 1/9 monolayer H-coverage is in close agreement with the value reported by Esposito *et al*. [81] and so we do not apply any additional corrections (shifts) to the HBE.

In Figure 8, we display all sites of the $MoSe_2$ electrocatalyst (pristine or doped) which lie near Pt(111)—the "gold-standard" HER catalyst—and closer to the peak of the volcano plot; positions of other sites with relatively poor HER activities on this volcano plot are reported in Figure S13 for completeness. In accordance with previous studies,[11,12] we see that defect-free Mo edges and Se edges of undoped $MoSe_2$ are highly active for HER. For all TM-doped $MoSe_2$ cases considered here, Se vacancy sites on Se edges and within the basal plane emerge as new active sites for HER, and they are likely to have equal or better HER activities than their respective counterparts in undoped $MoSe_2$. Specifically, a Se vacancy in the Fe-doped Se edge (θ_{Se}=1.0) has nearly optimal HBE for facile HER; defect-free Se and Mo edges of TM-doped $MoSe_2$, on the other hand, do not show improved HER activities, and among all defect-free doped edge sites, only Fe-doped Se-edges (θ_{Se}=1.0) retain high HER activity. The most important observation from Figure 8 is that *all* dopants render Se vacancy sites on the basal plane more active for HER: with Co-doping, basal plane Se vacancies become highly active for HER and, with Ni doping, both basal plane Se

vacancies and Se on-top sites (defect-free case) become highly active for HER. Thus, based on the volcano plot analysis, we conclude that Co and Ni are highly promising candidates for enhancing the electrocatalytic activity of $MoSe_2$ towards HER, as these dopants activate the *basal plane*, which constitutes most of the surface area of the 2D material.

As mentioned in the introduction, many previous studies[8,11,12,22,28–30] have also modified TMDs like MoS_2, $MoSe_2$, WS_2, and WSe_2 with various TM-dopants and improved their respective catalytic activities for HER. However, further experiments are needed for a comprehensive and systematic comparison of HER activities of various TM-doped TMDs and to identify clearly the relevant active sites for HER. Our theoretical calculations can thus provide some insights into designing such experiments in the future.

5. CONCLUSIONS

Using first principles DFT calculations, we investigated select electron-rich transition-metal (TM) dopants—Mn, Fe, Co, and Ni—for the activation of $MoSe_2$ towards electrochemical hydrogen evolution reaction (HER) in acidic media. The key findings of our study may be summarized as follows:

(1) The selected TM dopants introduce excess electrons in $MoSe_2$ and modify the electronic structure of the inert semiconducting basal plane, making it slightly more conducive—although far from ideal—for HER. Specifically, TM dopants increase the density of half-filled *p*-states near the Fermi level and enable the formation of stronger Se-H bonds. Ni doping is the one promising case for basal plane activation, as H adsorption actually becomes thermodynamically favorable at nearest-neighbor Se top sites in the defect-free basal plane, and these Se top sites are potentially highly active towards HER. Thus, Ni

doping might be a broadly applicable strategy for activating the large basal planes of TMDs although the occurrence of such sites might be small due to the high energy of substitution (Table S2).

(2) All TM dopants studied here can activate the basal plane by promoting the formation of HER-active Se vacancies in the $MoSe_2$ basal plane via the electrochemical deselenization reaction (DSR) at relatively small cathodic potentials. Se vacancy formation becomes thermodynamically more feasible in TM-doped basal planes due to the combination of electronic destabilization of the Se atom adjacent to th

(3) e electron-rich TM dopants and weakening of the metal-Se bond upon H adsorption. The overall ordering of HER activity at the basal plane (BSL) Se vacancies (V_{Se}) is $V_{Se}, \mathrm{Ni}-\mathrm{BSL} > V_{Se}, \mathrm{Co}-\mathrm{BSL} > V_{Se}, \mathrm{Mo}-\mathrm{BSL} > V_{Se}, \mathrm{Mn}-\mathrm{BSL} > V_{Se}, \mathrm{Fe}-\mathrm{BSL}$ (Figure 8).

(4) $MoSe_2$ edges undergo significant relaxation and reconstruction with doping and these effects can be as, if not more, energetically relevant than purely electronic considerations. Consequently, the details of the edge structure become important when examining the thermodynamics of HER and DSR on both Se and Mo edges of $MoSe_2$. The influence of TM dopants on the HER activity of defect-free Se and Mo edges is not favorable because TM doping typically results in underbinding of H at these edges. DSR, on the other hand, becomes thermodynamically favorable at the much smaller cathodic potentials for TM-doped Se and Mo edges. Se vacancies are highly active for HER at Se edges but are undesirable at Mo edges, requiring larger cathodic potentials for activation. Nevertheless, since the formation of Se vacancies at Mo edges requires larger limiting potentials than at the Se edges, it might be possible to generate these desirable Se vacancies preferentially at Se edges by working within a suitable window of cathodic potentials. The overall ordering

of HER activity at the Mo- and Se- edges, with or without Se vacancies (V_{Se}) is $V_{Se}, Fe-Se-edge > V_{Se}, Ni-Se-edge > V_{Se}, Mn-Se-edge > V_{Se}, Co-Se-edge > Mo-edge > Se-edge = Fe-Se-edge$ (Figure 8).

In summary, our results suggest several potential avenues for activating semiconducting $MoSe_2$, and possibly other TMDs, via substitutional doping with electron-rich dopants. Most importantly, several of the doped structures studied here are potentially as, if not more, active than Pt(111) and thus hold promise for economical electrochemical water splitting.

ACKNOWLEDGEMENTS

We gratefully acknowledge research support from the National Science Foundation (NSF-CBET-1803614) and the United States–Israel Binational Science Foundation (NSF-BSF CBET 2017642). This work used the Extreme Science and Engineering Discovery Environment (XSEDE), which is supported by National Science Foundation grant number ACI-1548562.

Supporting Information

Optimized structural models of doped and undoped $MoSe_2$ electrocatalysts before and after H adsorption; Energetics of TM-doping of $MoSe_2$ basal plane, and edges; Relative thermodynamic stability of Se coverage on Mo edge; Effects of TM-doping on the local structure of $MoSe_2$ basal plane, and; Electronic structure of the Se and adsorbed H atom in undoped and doped $MoSe_2$ basal plane; Electronic structure of the HER sites on doped and undoped $MoSe_2$ edges; Free-energy diagrams for HER and DSR on doped and undoped $MoSe_2$ basal plane and edges; HER volcano plot with all sites of the doped and undoped $MoSe_2$ electrocatalyst.

REFERENCES

(1) Seh, Z. W.; Kibsgaard, J.; Dickens, C. F.; Chorkendorff, I. B.; Nørskov, J. K.; Jaramillo, T. F. Combining Theory and Experiment in Electrocatalysis: Insights into Materials Design. *Science (80-.).* **2017**, *355* (6321), eaad4998.

(2) Turner, J. A. Sustainable Hydrogen Production. *Science (80-.).* **2004**, *305* (5686), 972–974.

(3) Kibler, L. A. Hydrogen Electrocatalysis. *ChemPhysChem* **2006**, *7* (5), 985–991.

(4) Vesborg, P. C. K.; Seger, B.; Chorkendorff, I. Recent Development in Hydrogen Evolution Reaction Catalysts and Their Practical Implementation. *J. Phys. Chem. Lett.* **2015**, *6* (6), 951–957.

(5) Zhao, G.; Rui, K.; Dou, S. X.; Sun, W. Heterostructures for Electrochemical Hydrogen Evolution Reaction: A Review. *Adv. Funct. Mater.* **2018**, *28* (43), 1803291.

(6) Esposito, D. V; Chen, J. G. Monolayer Platinum Supported on Tungsten Carbides as Low-Cost Electrocatalysts: Opportunities and Limitations. *Energy Environ. Sci.* **2011**, *4* (10), 3900–3912.

(7) Kangasniemi, K. H.; Condit, D. A.; Jarvi, T. D. Characterization of Vulcan Electrochemically Oxidized under Simulated PEM Fuel Cell Conditions. *J. Electrochem. Soc.* **2004**, *151* (4), E125.

(8) Zhang, K.; Li, Y.; Deng, S.; Shen, S.; Zhang, Y.; Pan, G.; Xiong, Q.; Liu, Q.; Xia, X.; Wang, X. Molybdenum Selenide Electrocatalysts for Electrochemical Hydrogen Evolution Reaction. *ChemElectroChem* **2019**, *6* (14), 3530–3548.

(9) Tsai, C.; Chan, K.; Abild-Pedersen, F.; Nørskov, J. K. Active Edge Sites in MoSe $_2$ and WSe $_2$ Catalysts for the Hydrogen Evolution Reaction: A Density Functional Study. *Phys. Chem. Chem. Phys.* **2014**, *16* (26), 13156–13164.

(10) Hinnemann, B.; Moses, P. G.; Bonde, J.; Jørgensen, K. P.; Nielsen, J. H.; Horch, S.; Chorkendorff, I.; Nørskov, J. K. Biomimetic Hydrogen Evolution: MoS2 Nanoparticles as Catalyst for Hydrogen Evolution. *J. Am. Chem. Soc.* **2005**, *127* (15), 5308–5309.

(11) Kong, D.; Wang, H.; Cha, J. J.; Pasta, M.; Koski, K. J.; Yao, J.; Cui, Y. Synthesis of MoS2 and MoSe2 Films with Vertically Aligned Layers. *Nano Lett.* **2013**, *13* (3), 1341–1347.

(12) Wang, H.; Kong, D.; Johanes, P.; Cha, J. J.; Zheng, G.; Yan, K.; Liu, N.; Cui, Y. MoSe2and WSe2nanofilms with Vertically Aligned Molecular Layers on Curved and Rough Surfaces. *Nano Lett.* **2013**, *13* (7), 3426–3433.

(13) Voiry, D.; Yamaguchi, H.; Li, J.; Silva, R.; Alves, D. C. B.; Fujita, T.; Chen, M.; Asefa, T.; Shenoy, V. B.; Eda, G. Enhanced Catalytic Activity in Strained Chemically Exfoliated WS 2 Nanosheets for Hydrogen Evolution. *Nat. Mater.* **2013**, *12* (9), 850.

(14) Wang, Q. H.; Kalantar-Zadeh, K.; Kis, A.; Coleman, J. N.; Strano, M. S. Electronics and Optoelectronics of Two-Dimensional Transition Metal Dichalcogenides. *Nat. Nanotechnol.* **2012**, *7* (11), 699.

(15) Chia, X.; Eng, A. Y. S.; Ambrosi, A.; Tan, S. M.; Pumera, M. Electrochemistry of Nanostructured Layered Transition-Metal Dichalcogenides. *Chem. Rev.* **2015**, *115* (21), 11941–11966.

(16) Jaramillo, T. F.; Jørgensen, K. P.; Bonde, J.; Nielsen, J. H.; Horch, S.; Chorkendorff, I. Identification of Active Edge Sites for Electrochemical H2 Evolution from MoS2 Nanocatalysts. *Science (80-.).* **2007**, *317* (5834), 100–102.

(17) Ambrosi, A.; Sofer, Z.; Pumera, M. 2H→ 1T Phase Transition and Hydrogen Evolution Activity of MoS 2, MoSe 2, WS 2 and WSe 2 Strongly Depends on the MX 2 Composition. *Chem. Commun.* **2015**, *51* (40), 8450–8453.

(18) Ravikumar, C. H.; Nair, G. V.; Muralikrishna, S.; Nagaraju, D. H.; Balakrishna, R. G. Nanoflower like Structures of MoSe2 and MoS2 as Efficient Catalysts for Hydrogen Evolution. *Mater. Lett.* **2018**, *220*, 133–135.

(19) Tang, H.; Dou, K.; Kaun, C.-C.; Kuang, Q.; Yang, S. $MoSe_2$ Nanosheets and Their Graphene Hybrids: Synthesis, Characterization and Hydrogen Evolution Reaction Studies. *J. Mater. Chem. A* **2014**, *2* (2), 360–364.

(20) Gholamvand, Z.; McAteer, D.; Backes, C.; McEvoy, N.; Harvey, A.; Berner, N. C.; Hanlon, D.; Bradley, C.; Godwin, I.; Rovetta, A.; et al. Comparison of Liquid Exfoliated Transition Metal Dichalcogenides Reveals $MoSe_2$ to Be the Most Effective Hydrogen Evolution Catalyst. *Nanoscale* **2016**, *8* (10), 5737–5749.

(21) Jin, H.; Guo, C.; Liu, X.; Liu, J.; Vasileff, A.; Jiao, Y.; Zheng, Y.; Qiao, S.-Z. Emerging Two-Dimensional Nanomaterials for Electrocatalysis. *Chem. Rev.* **2018**, acs.chemrev.7b00689.

(22) Tsai, C.; Li, H.; Park, S.; Park, J.; Han, H. S.; Nørskov, J. K.; Zheng, X.; Abild-Pedersen, F. Electrochemical Generation of Sulfur Vacancies in the Basal Plane of MoS 2 for Hydrogen Evolution. *Nat. Commun.* **2017**, *8*, 15113.

(23) Lin, S.-H.; Kuo, J.-L. Activating and Tuning Basal Planes of MoO 2, MoS 2, and MoSe 2 for Hydrogen Evolution Reaction. *Phys. Chem. Chem. Phys.* **2015**, *17* (43), 29305–29310.

(24) Li, H.; Tsai, C.; Koh, A. L.; Cai, L.; Contryman, A. W.; Fragapane, A. H.; Zhao, J.; Han, H. S.; Manoharan, H. C.; Abild-Pedersen, F. Activating and Optimizing MoS 2 Basal Planes for Hydrogen Evolution through the Formation of Strained Sulphur Vacancies. *Nat. Mater.* **2016**, *15* (1), 48.

(25) Ouyang, Y.; Ling, C.; Chen, Q.; Wang, Z.; Shi, L.; Wang, J. Activating Inert Basal Planes of MoS2 for Hydrogen Evolution Reaction through the Formation of Different Intrinsic Defects. *Chem. Mater.* **2016**, *28* (12), 4390–4396.

(26) Lee, J.; Kang, S.; Yim, K.; Kim, K. Y.; Jang, H. W.; Kang, Y.; Han, S. Hydrogen Evolution Reaction at Anion Vacancy of Two-Dimensional Transition-Metal Dichalcogenides: Ab Initio Computational Screening. *J. Phys. Chem. Lett.* **2018**, *9* (8), 2049–2055.

(27) Shu, H.; Zhou, D.; Li, F.; Cao, D.; Chen, X. Defect Engineering in MoSe2 for the Hydrogen Evolution Reaction: From Point Defects to Edges. *ACS Appl. Mater. Interfaces* **2017**, *9* (49), 42688–42698.

(28) Zhao, G.; Rui, K.; Dou, S. X.; Sun, W. Heterostructures for Electrochemical Hydrogen Evolution Reaction: A Review. *Adv. Funct. Mater.* **2018**, *1803291*, 1803291.

(29) Xie, J.; Zhang, J.; Li, S.; Grote, F.; Zhang, X.; Zhang, H.; Wang, R.; Lei, Y.; Pan, B.; Xie, Y. Controllable Disorder Engineering in Oxygen-Incorporated MoS2 Ultrathin Nanosheets for Efficient Hydrogen Evolution. *J. Am. Chem. Soc.* **2013**, *135* (47), 17881–17888.

(30) Luo, P.; Zhuge, F.; Zhang, Q.; Chen, Y.; Lv, L.; Huang, Y.; Li, H.; Zhai, T. Doping Engineering and Functionalization of Two-Dimensional Metal Chalcogenides. *Nanoscale Horizons* **2019**, *4* (1), 26–51.

(31) Zhou, X.; Jiang, J.; Ding, T.; Zhang, J.; Pan, B.; Zuo, J.; Yang, Q. Fast Colloidal Synthesis of Scalable Mo-Rich Hierarchical Ultrathin MoSe 2− x Nanosheets for High-Performance Hydrogen Evolution. *Nanoscale* **2014**, *6* (19), 11046–11051.

(32) Grigoriev, S. N.; Fominski, V. Y.; Romanov, R. I.; Volosova, M. A.; Shelyakov, A. V. Pulsed Laser Deposition of Nanocomposite MoSex/Mo Thin-Film Catalysts for Hydrogen Evolution Reaction. *Thin Solid Films* **2015**, *592*, 175–181.

(33) Kuraganti, V.; Jain, A.; Bar-Ziv, R.; Ramasubramaniam, A.; Bar-Sadan, M. Manganese Doping of MoSe2 Promotes Active Defect Sites for Hydrogen Evolution. *ACS Appl. Mater. Interfaces* **2019**, *11* (28), 25155–25162.

(34) Vasu, K.; Meiron, O. E.; Enyashin, A. N.; Bar-Ziv, R.; Bar-Sadan, M. Effect of Ru Doping on the Properties of MoSe2 Nanoflowers. *J. Phys. Chem. C* **2019**, *123* (3), 1987–1994.

(35) Lei, Z.; Xu, S.; Wu, P. Ultra-Thin and Porous MoSe 2 Nanosheets: Facile Preparation and Enhanced Electrocatalytic Activity towards the Hydrogen Evolution Reaction. *Phys. Chem. Chem. Phys.* **2016**, *18* (1), 70–74.

(36) Deng, S.; Yang, F.; Zhang, Q.; Zhong, Y.; Zeng, Y.; Lin, S.; Wang, X.; Lu, X.; Wang, C.; Gu, L. Phase Modulation of (1T-2H)-MoSe2/TiC-C Shell/Core Arrays via Nitrogen Doping for Highly Efficient Hydrogen Evolution Reaction. *Adv. Mater.* **2018**, *30* (34), 1802223.

(37) Deng, S.; Zhong, Y.; Zeng, Y.; Wang, Y.; Yao, Z.; Yang, F.; Lin, S.; Wang, X.; Lu, X.; Xia, X. Directional Construction of Vertical Nitrogen-Doped 1T-2H MoSe2/Graphene Shell/Core Nanoflake Arrays for Efficient Hydrogen Evolution Reaction. *Adv. Mater.* **2017**, *29* (21), 1700748.

(38) Zhang, J.; Wang, T.; Liu, P.; Liu, Y.; Ma, J.; Gao, D. Enhanced Catalytic Activities of Metal-Phase-Assisted 1T@ 2H-MoSe2 Nanosheets for Hydrogen Evolution. *Electrochim. Acta* **2016**, *217*, 181–186.

(39) Zhu, M.; Luo, Z.; Pan, A.; Yang, H.; Zhu, T.; Liang, S.; Cao, G. N-Doped One-Dimensional Carbonaceous Backbones Supported MoSe2 Nanosheets as Superior Electrodes for Energy Storage and Conversion. *Chem. Eng. J.* **2018**, *334*, 2190–2200.

(40) Park, G. D.; Kim, J. H.; Park, S.-K.; Kang, Y. C. MoSe2 Embedded CNT-Reduced Graphene Oxide Composite Microsphere with Superior Sodium Ion Storage and Electrocatalytic Hydrogen Evolution Performances. *ACS Appl. Mater. Interfaces* **2017**, *9* (12), 10673–10683.

(41) Mao, S.; Wen, Z.; Ci, S.; Guo, X.; Ostrikov, K.; Chen, J. Perpendicularly Oriented MoSe2/Graphene Nanosheets as Advanced Electrocatalysts for Hydrogen Evolution. *Small* **2015**, *11* (4), 414–419.

(42) Gong, Q.; Cheng, L.; Liu, C.; Zhang, M.; Feng, Q.; Ye, H.; Zeng, M.; Xie, L.; Liu, Z.; Li, Y. Ultrathin MoS2(1–x)Se2x Alloy Nanoflakes For Electrocatalytic Hydrogen Evolution Reaction. *ACS Catal.* **2015**, *5* (4), 2213–2219.

(43) Meiron, O. E.; Houben, L.; Bar-Sadan, M. Understanding the Formation Mechanism and the 3D Structure of Mo (S x Se 1− x) 2 Nanoflowers. *RSC Adv.* **2015**, *5* (107), 88108–

88114.

(44) Gao, D.; Xia, B.; Zhu, C.; Du, Y.; Xi, P.; Xue, D.; Ding, J.; Wang, J. Activation of the MoSe2basal Plane and Se-Edge by B Doping for Enhanced Hydrogen Evolution. *J. Mater. Chem. A* **2018**, *6* (2), 510–515.

(45) Meiron, O. E.; Kuraganti, V.; Hod, I.; Bar-Ziv, R.; Bar-Sadan, M. Improved Catalytic Activity of Mo 1− x W x Se 2 Alloy Nanoflowers Promotes Efficient Hydrogen Evolution Reaction in Both Acidic and Alkaline Aqueous Solutions. *Nanoscale* **2017**, *9* (37), 13998–14005.

(46) Zhao, G.; Wang, X.; Wang, S.; Rui, K.; Chen, Y.; Yu, H.; Ma, J.; Dou, S. X.; Sun, W. Heteroatom-doped MoSe2 Nanosheets with Enhanced Hydrogen Evolution Kinetics for Alkaline Water Splitting. *Chem. Asian J.* **2019**, *14* (2), 301–306.

(47) Qian, J.; Wang, T.; Xia, B.; Xi, P.; Gao, D. Zn-Doped MoSe2 Nanosheets as High-Performance Electrocatalysts for Hydrogen Evolution Reaction in Acid Media. *Electrochim. Acta* **2019**, *296*, 701–708.

(48) Vikraman, D.; Hussain, S.; Akbar, K.; Karuppasamy, K.; Chun, S.-H.; Jung, J.; Kim, H.-S. Design of Basal Plane Edges in Metal-Doped Nanostripes-Structured MoSe2 Atomic Layers to Enhance Hydrogen Evolution Reaction Activity. *ACS Sustain. Chem. Eng.* **2018**, *7* (1), 458–469.

(49) Chen, X.; Qiu, Y.; Liu, G.; Zheng, W.; Feng, W.; Gao, F.; Cao, W.; Fu, Y.; Hu, W.; Hu, P. Tuning Electrochemical Catalytic Activity of Defective 2D Terrace MoSe 2 Heterogeneous Catalyst via Cobalt Doping. *J. Mater. Chem. A* **2017**, *5* (22), 11357–11363.

(50) Yang, Y.; Zhao, X.; Mao, H.; Ning, R.; Zheng, X.; Sui, J.; Cai, W. Nickel-Doped MoSe2 Nanosheets with Ni–Se Bond for Alkaline Electrocatalytic Hydrogen Evolution. *Int. J. Hydrogen Energy* **2020**.

(51) Zimron, O.; Zilberman, T.; Kadam, S. R.; Ghosh, S.; Kolatker, S.; Neyman, A.; Bar-Ziv, R.; Bar-Sadan, M. Co-doped MoSe2 Nanoflowers as Efficient Catalysts for Electrochemical Hydrogen Evolution Reaction (HER) in Acidic and Alkaline Media. *Isr. J. Chem.* **2020**.

(52) Park, S.; Park, J.; Abroshan, H.; Zhang, L.; Kim, J. K.; Zhang, J.; Guo, J.; Siahrostami, S.; Zheng, X. Enhancing Catalytic Activity of MoS2 Basal Plane S-Vacancy by Co Cluster Addition. *ACS Energy Lett.* **2018**, *3* (11), 2685–2693.

(53) Li, G.; Fu, C.; Wu, J.; Rao, J.; Liou, S.-C.; Xu, X.; Shao, B.; Liu, K.; Liu, E.; Kumar, N. Synergistically Creating Sulfur Vacancies in Semimetal-Supported Amorphous MoS2 for Efficient Hydrogen Evolution. *Appl. Catal. B Environ.* **2019**, *254*, 1–6.

(54) Kresse, G.; Furthmüller, J. Efficient Iterative Schemes for Ab Initio Total-Energy Calculations Using a Plane-Wave Basis Set. *Phys. Rev. B* **1996**, *54* (16), 11169–11186.

(55) Kresse, G.; Furthmüller, J. Efficiency of Ab-Initio Total Energy Calculations for Metals and Semiconductors Using a Plane-Wave Basis Set. *Comput. Mater. Sci.* **1996**, *6* (1), 15–50.

(56) Blöchl, P. E. Projector Augmented-Wave Method. *Phys. Rev. B* **1994**, *50* (24), 17953–17979.

(57) Kresse, G.; Joubert, D. From Ultrasoft Pseudopotentials to the Projector Augmented-

Wave Method. *Phys. Rev. B* **1999**, *59* (3), 1758–1775.

(58) Perdew, J. P.; Burke, K.; Ernzerhof, M. Generalized Gradient Approximation Made Simple. *Phys. Rev. Lett.* **1996**, *77* (18), 3865–3868.

(59) Bollinger, M. V; Jacobsen, K. W.; No, J. K.; Mos, E. Atomic and Electronic Structure of MoS 2 Nanoparticles. **2003**, No. June 2002, 1–17.

(60) Byskov, L. S.; Nørskov, J. K.; Clausen, B. S.; Topsøe, H. DFT Calculations of Unpromoted and Promoted MoS2-Based Hydrodesulfurization Catalysts. *J. Catal.* **1999**, *187* (1), 109–122.

(61) Bollinger, M. V; Lauritsen, J. V; Jacobsen, K. W.; Nørskov, J. K.; Helveg, S.; Besenbacher, F. One-Dimensional Metallic Edge States in MoS 2. *Phys. Rev. Lett.* **2001**, *87* (19), 196803.

(62) Brixner, L. H. Preparation and Properties of the Single Crystalline AB2-Type Selenides and Tellurides of Niobium, Tantalum, Molybdenum and Tungsten. *J. Inorg. Nucl. Chem.* **1962**, *24* (3), 257–263.

(63) Makov, G.; Payne, M. C. Periodic Boundary Conditions in Ab Initio Calculations. *Phys. Rev. B* **1995**, *51* (7), 4014.

(64) Jain, A.; Ramasubramaniam, A. Tuning Core–Shell Interactions in Tungsten Carbide–Pt Nanoparticles for the Hydrogen Evolution Reaction. *Phys. Chem. Chem. Phys.* **2018**, *20* (36), 23262–23271.

(65) Reuter, K.; Stampf, C.; Scheffler, M. Ab Initio Atomistic Thermodynamics and Statistical Mechanics of Surface Properties and Functions. In *Handbook of materials modeling*; Springer, 2005; pp 149–194.

(66) Johnson III, R. D. *NIST 101. Computational Chemistry Comparison and Benchmark Database*; 1999.

(67) Wang, H.; Tsai, C.; Kong, D.; Chan, K.; Abild-Pedersen, F.; Nørskov, J. K.; Cui, Y. Transition-Metal Doped Edge Sites in Vertically Aligned MoS 2 Catalysts for Enhanced Hydrogen Evolution. *Nano Res.* **2015**, *8* (2), 566–575.

(68) Hakala, M.; Kronberg, R.; Laasonen, K. Hydrogen Adsorption on Doped MoS 2 Nanostructures. *Sci. Rep.* **2017**, *7* (1), 15243.

(69) Tsai, C.; Chan, K.; Nørskov, J. K.; Abild-Pedersen, F. Rational Design of MoS 2 Catalysts: Tuning the Structure and Activity via Transition Metal Doping. *Catal. Sci. Technol.* **2015**, *5* (1), 246–253.

(70) Gao, G.; Jiao, Y.; Ma, F.; Jiao, Y.; Waclawik, E.; Du, A. Charge Mediated Semiconducting-to-Metallic Phase Transition in Molybdenum Disulfide Monolayer and Hydrogen Evolution Reaction in New 1T′ Phase. *J. Phys. Chem. C* **2015**, *119* (23), 13124–13128.

(71) Dungey, K. E.; Curtis, M. D.; Penner-Hahn, J. E. Structural Characterization and Thermal Stability of MoS2 Intercalation Compounds. *Chem. Mater.* **1998**, *10* (8), 2152–2161.

(72) Chhowalla, M.; Shin, H. S.; Eda, G.; Li, L.-J.; Loh, K. P.; Zhang, H. The Chemistry of Two-Dimensional Layered Transition Metal Dichalcogenide Nanosheets. *Nat. Chem.* **2013**, *5* (4), 263.

(73) Nørskov, J. K.; Bligaard, T.; Logadottir, a.; Kitchin, J. R.; Chen, J. G.; Pandelov, S.; Stimming, U. Trends in the Exchange Current for Hydrogen Evolution. *J. Electrochem.*

Soc. **2005**, *152* (3), J23.

(74) Greeley, J.; Jaramillo, T. F.; Bonde, J.; Chorkendorff, I. B.; Nørskov, J. K. Computational High-Throughput Screening of Electrocatalytic Materials for Hydrogen Evolution. *Nat. Mater.* **2006**, *5* (11), 909–913.

(75) Sabatier, P. *Catalysis in Organic Chemistry*; D. Van Nostrand Company, 1922.

(76) Parsons, R. The Rate of Electrolytic Hydrogen Evolution and the Heat of Adsorption of Hydrogen. *Trans. Faraday Soc.* **1958**, *54* (0), 1053–1063.

(77) Lin, Z.; Carvalho, B. R.; Kahn, E.; Lv, R.; Rao, R.; Terrones, H.; Pimenta, M. A.; Terrones, M. Defect Engineering of Two-Dimensional Transition Metal Dichalcogenides. *2D Mater.* **2016**, *3* (2), 22002.

(78) Ma, Q.; Odenthal, P. M.; Mann, J.; Le, D.; Wang, C. S.; Zhu, Y.; Chen, T.; Sun, D.; Yamaguchi, K.; Tran, T. Controlled Argon Beam-Induced Desulfurization of Monolayer Molybdenum Disulfide. *J. Phys. Condens. Matter* **2013**, *25* (25), 252201.

(79) Nørskov, J. K.; Rossmeisl, J.; Logadottir, A.; Lindqvist, L.; Kitchin, J. R.; Bligaard, T.; Jónsson, H. Origin of the Overpotential for Oxygen Reduction at a Fuel-Cell Cathode. *J. Phys. Chem. B* **2004**, *108* (46), 17886–17892.

(80) Tsai, C.; Abild-Pedersen, F.; Nørskov, J. K. Tuning the MoS2 Edge-Site Activity for Hydrogen Evolution via Support Interactions. *Nano Lett.* **2014**, *14* (3), 1381–1387.

(81) Esposito, D. V.; Hunt, S. T.; Kimmel, Y. C.; Chen, J. G. A New Class of Electrocatalysts for Hydrogen Production from Water Electrolysis: Metal Monolayers Supported on Low-Cost Transition Metal Carbides. *J. Am. Chem. Soc.* **2012**, *134* (6), 3025–3033.

(82) Ling, C.; Ouyang, Y.; Shi, L.; Yuan, S.; Chen, Q.; Wang, J. Template-Grown MoS2 Nanowires Catalyze the Hydrogen Evolution Reaction: Ultralow Kinetic Barriers with High Active Site Density. *ACS Catal.* **2017**, *7* (8), 5097–5102.

(83) Tsai, C.; Chan, K.; Nørskov, J. K.; Abild-Pedersen, F. Theoretical Insights into the Hydrogen Evolution Activity of Layered Transition Metal Dichalcogenides. *Surf. Sci.* **2015**, *640*, 133–140.

(84) Tang, Q.; Jiang, D. Mechanism of Hydrogen Evolution Reaction on 1T-MoS2 from First Principles. *Acs Catal.* **2016**, *6* (8), 4953–4961.

Table of Contents Figure